

# Stability, dynamical properties and melting of a classical bi-layer Wigner Crystal

G. Goldoni\* and F. M. Peeters†

*Departement Natuurkunde, Universiteit Antwerpen (UIA), Universiteitsplein 1, B-2610  
Antwerpen, Belgium  
(October 7, 2018)*

## Abstract

We investigate the stability, the dynamical properties and melting of a two-dimensional (2D) Wigner crystal (WC) of classical Coulombic particles in a bi-layer structure. Compared to the single-layer WC, this system shows a rich phase diagram. Five different crystalline phases are stable; the energetically favoured structure can be tuned by changing either the inter-layer distance or the particle density. Phase boundaries consist of both continuous and discontinuous transitions. We calculated the phonon excitations of the system within the harmonic approximation and we evaluated the melting temperature of the bi-layer WC by use of a modified Lindemann criterion, appropriate to 2D systems. We minimized the harmonic free-energy of the system with respect to the lattice geometry at different values of temperature/inter-layer distance and we found no temperature-induced structural phase transition.

68.65.+g – Layer structures: multilayer, and superlattices

63.20.Dj – Phonon states and bands, normal modes, and phonon dispersion

64.70.Dv – Solid-liquid transitions

## INTRODUCTION

Classical charged particles confined in a single, two-dimensional (2D) layer localize into a hexagonal lattice (Wigner crystal) for sufficiently large densities and low temperatures.<sup>1</sup> Such a single-layer Wigner crystal (SLWC) has been realized, e.g., on the surface of liquid helium.<sup>2</sup> Colloidal particles dissolved in water and placed between two glass plates is another example of an experimental system where classical particles exhibit Wigner crystallization.<sup>3</sup> Electrons in 2D semiconductor heterostructures behave like quantum particles, but a strong perpendicular magnetic field quenches the kinetic energy, leading the system toward the classical regime. The quest for the observation of such a Wigner crystal has been the object of very intense work over the last decades.<sup>4</sup> The melting transition of the classical SLWC, in particular, has attracted a large body of investigation<sup>5</sup> since the proposal of a dislocation-mediated melting mechanism, leading to the prediction of a continuous melting transition.<sup>6–8</sup>

Recently, a new 2D system has attracted the attention of several groups, namely, the Wigner crystal in a bi-layer structure. One of the peculiarities of the bi-layer Wigner crystal (BLWC), compared to the SLWC, consists in the rich phase diagram; it has been predicted that different crystalline structures are stable in different ranges of inter-layer distance/charge density.<sup>9–15</sup>

In the present paper we address the phase diagram of such bi-layer structures.<sup>13</sup> We consider a BLWC of Coulombic particles evenly distributed between the two layers. In a classical BLWC, the inter-particle interaction can be characterized by a unique dimensionless parameter  $\eta = d\sqrt{n/2}$ , where  $d$  is the inter-layer distance and  $n$  is the total charge density.  $\eta$  represents the ratio between the inter-particle interaction *between* the layer and *within* each layer. Thus, in the classical case, the Hamiltonian of the system is only a function of  $\eta$ , which therefore determines completely the phase diagram at  $T = 0$ . This is in contrast with the equivalent quantum problem, where  $d$  and  $n$  do not scale out. The search for the stable structure of a classical BLWC, at  $T = 0$  and as a function of  $\eta$ , is made easier by the following considerations: 1) due to the long-range interaction, the two lattices which occupy the two layers (sub-lattices) are staggered to maximize the inter-particle distance. Each lattice site sits at the center of a cell in the opposite layer; 2) there are two trivial limiting cases: at  $\eta = 0$  the two sub-lattices reduce to a SLWC, which is known to crystallize in a hexagonal lattice (one-component hexagonal lattice). At the opposite limit of large  $\eta$  the two sub-lattices are weakly coupled and, therefore, the stable structure is constituted by two staggered SLWC (staggered hexagonal lattice). By comparing the static energy of several lattices, we find that five different phases are energetically favoured in different ranges of  $\eta$ . The five structures, in order of increasing  $\eta$ , are a one-component hexagonal lattice (I), a staggered rectangular lattice (II), a staggered square lattice (III), a staggered rhombic lattice (IV), and a staggered hexagonal lattice (V). These phases evolve one into the other through both first and second order phase transitions.

There exist already a number of investigations of the  $T = 0$  phase diagram of the classical BLWC in various systems.<sup>9,11–13,15</sup> Some of the previous investigations of the present system<sup>11,15</sup> did not identify all five phases. In Ref. 12, the bi-layer electron system which forms in a single wide quantum well above a critical density<sup>16</sup> was studied. In this case, the transition from the single layer to the bi-layer (and, at higher densities, to a higher

number of layers) is of first order, with  $\eta$  which jumps from 0 to  $\sim 0.27$ ; therefore, the low- $\eta$  phases I and II were not investigated in Ref. 12. Theoretical investigations suggest that also bi-layer structures in the quantum regime possess a complex phase diagram. In Ref. 17 a structural instability is found in the strong coupling regime, when the tunneling probability decreases below a critical threshold as a consequence of layer separation. The five phases described above have been predicted to exist in a bi-layer quantum Hall system.<sup>14</sup> In this case, the phase diagram is even more complex, because a spin structure is associated with the lattice structure. Other bi-layer structures with an even more complex phase diagram can be imagined, for example, with different densities of the two layers.<sup>9,10</sup>

Phonon excitations of some of the above systems have been partially investigated, within the harmonic approximation.<sup>11,12,15</sup> Phonon frequencies have been used to evaluate the zero-point energy and the critical density for cold melting of the quantum BLWC<sup>12,15</sup> also in the presence of a magnetic field.

In this paper we address the *non-zero* temperature phase diagram of a classical BLWC, which has not been investigated so far. With this aim, we have systematically investigated, within the harmonic approximation, the phonon excitations of each of the five structures. This allowed us not only to determine the range of structural stability and the behaviour of the acoustical and optical modes, which could be subject to experimental observations, but also allowed us to estimate the melting temperature of the crystal through the Lindemann criterion. The latter states that melting takes place when the mean square displacement of the crystallized charges exceeds a certain fraction of the lattice parameter. It should be noted that in 2D the mean square displacement diverges logarithmically with the crystal size. On the other hand, the *relative* mean square displacement between nearest neighbours (NN's) is a well defined quantity and its value at melting has been determined from simulations of 2D crystals.<sup>18</sup> Therefore, the latter quantity has been used in the present paper to estimate the melting temperature. Our results show that, by changing  $\eta$  at constant temperature, one can pass through alternating regions of crystalline and liquid order.

The overlapping range of stability of different lattice structures along the  $\eta$  axis suggests the possibility that temperature-induced structural phase transitions take place, before the melting temperature is reached. To investigate this last possibility, we have minimized the harmonic free-energy of different structures at increasing temperatures at fixed  $\eta$ , and we have found no evidence of such a temperature-induced structural phase transition.

The paper is organized as follows. In Sec. I we investigate the zero temperature phase diagram. In Sec. II we calculate the phonon excitations of the systems. The non-zero temperature phase diagram is investigated in Sec. III. Results are discussed and summarized in the last section.

## I. ZERO TEMPERATURE PHASE DIAGRAM

We consider a BLWC consisting of  $N$  classical, spinless particles with total charge density  $n$ , evenly distributed over the two layers. The same form of the Coulombic interaction  $e^2/r$  is assumed between particles in the same layer and in different layers.

Electrons crystallized in the two layers constitute two sub-lattices which are equivalent by symmetry. When necessary, we denote the two sub-lattices by A and B. We consider

only the case of two layers of equal charge density  $n_s = n/2$  each; therefore, in the limit  $\eta \rightarrow 0$ , we recover a SLWC of density  $n$ . We consider the BLWC as a 2D lattice of  $N/2$  unitary cells, with two electrons per cell sitting on opposite layers. The primitive vectors are denoted by  $\mathbf{a}_1$  and  $\mathbf{a}_2$ , and the basis vectors are  $(0, 0)$  and  $\mathbf{c}$ ;  $\mathbf{a}_1$ ,  $\mathbf{a}_2$ ,  $\mathbf{c}$ ,  $n_s$ , and the vectors  $\mathbf{b}_1$  and  $\mathbf{b}_2$  generating the reciprocal lattice, are listed in Table I for the five relevant phases. The equilibrium positions of the crystallized electrons in layer A and B are, respectively,

$$\mathbf{R}_A = i\mathbf{a}_1 + j\mathbf{a}_2 \quad (1)$$

$$\mathbf{R}_B = i\mathbf{a}_1 + j\mathbf{a}_2 + \mathbf{c} \quad (2)$$

where  $i, j$  are integers. The total potential energy of the mobile charges due to the intra-layer and the inter-layer interaction is

$$V_p = \frac{1}{2} \left\{ \sum_{\mathbf{R}_A \neq \mathbf{R}'_A} \frac{e^2}{|\mathbf{R}_A - \mathbf{R}'_A|} + \sum_{\mathbf{R}_B \neq \mathbf{R}'_B} \frac{e^2}{|\mathbf{R}_B - \mathbf{R}'_B|} + 2 \sum_{\mathbf{R}_A, \mathbf{R}_B} \frac{e^2}{[|\mathbf{R}_A - \mathbf{R}_B|^2 + d^2]^{1/2}} \right\}. \quad (3)$$

The factor  $1/2$  accounts for double counting. Since the two layers are equivalent, and the origin can be chosen arbitrarily if we neglect surface effects, there are  $N/2$  equivalent terms in each sum and the potential energy per particle  $E = V_p/N$ , therefore, reads

$$E = \frac{1}{2} (E_0 + E_I), \quad (4)$$

where

$$E_0 = \sum_{\mathbf{R} \neq 0} \frac{e^2}{R} \quad (5)$$

represents the intra-layer interaction energy, and

$$E_I = \sum_{\mathbf{R}} \frac{e^2}{[|\mathbf{R} + \mathbf{c}|^2 + d^2]^{1/2}} \quad (6)$$

is the inter-layer interaction energy. Here  $\mathbf{R} = i\mathbf{a}_1 + j\mathbf{a}_2$  and  $R = |\mathbf{R}|$ .

We follow Bonsall and Maradudin<sup>19</sup> and rewrite (5) as

$$E_0 = e^2 \lim_{r \rightarrow 0} \left[ \sum_{\mathbf{R}} \frac{1}{|\mathbf{r} - \mathbf{R}|} - \frac{1}{r} \right], \quad (7)$$

where  $\mathbf{r}$  is a 2D vector and  $r = |\mathbf{r}|$ . It is convenient to define the following two functions<sup>20</sup>

$$T_0(\mathbf{r}, \mathbf{q}) = e^{-i\mathbf{q} \cdot \mathbf{r}} \sum_{\mathbf{R}} \frac{e^{i\mathbf{q} \cdot (\mathbf{r} - \mathbf{R})}}{|\mathbf{r} - \mathbf{R}|} - \frac{1}{r}, \quad (8)$$

$$T_I(\mathbf{r}, \mathbf{q}) = e^{-i\mathbf{q} \cdot \mathbf{r}} \sum_{\mathbf{R}} \frac{e^{i\mathbf{q} \cdot (\mathbf{r} - \mathbf{R} + \mathbf{c})}}{[|\mathbf{r} - \mathbf{R} + \mathbf{c}|^2 + d^2]^{1/2}}, \quad (9)$$

from which  $E_0$  and  $E_I$  are obtained

$$E_0 = e^2 \lim_{r \rightarrow 0} T_0(\mathbf{r}, 0), \quad (10)$$

$$E_I = e^2 T_I(0, 0). \quad (11)$$

Due to the long range nature of the interaction, the lattice sums in  $T_0$  and  $T_I$  converge slowly. The Ewald technique is commonly used to overcome this difficulty, and consists in splitting the slowly convergent sum into two parts: the contribution of the first shells of neighbours is summed up in real space, while the contribution of the outer shells is summed up in reciprocal space. Both sums turn out to be rapidly convergent. The transformation to rapidly convergent sums over the real lattice vectors  $\mathbf{R}$  and the reciprocal lattice vectors  $\mathbf{G}$  is reported in Appendix A. Here we state the final result

$$\begin{aligned} T_0(\mathbf{r}, \mathbf{q}) = & \sqrt{n_s} \sum_{\mathbf{G}} e^{-i(\mathbf{q}+\mathbf{G})\cdot\mathbf{r}} \Phi\left(\frac{|\mathbf{q}+\mathbf{G}|^2}{4\pi n_s}\right) + \sqrt{n_s} \sum_{\mathbf{R} \neq 0} e^{-i\mathbf{q}\cdot\mathbf{R}} \Phi\left(\pi n_s |\mathbf{r} - \mathbf{R}|^2\right) \\ & + \sqrt{n_s} \Phi\left(\pi n_s r^2\right) - \frac{1}{r}, \end{aligned} \quad (12)$$

$$\begin{aligned} T_I(\mathbf{r}, \mathbf{q}) = & \sqrt{n_s} \sum_{\mathbf{G}} e^{-i(\mathbf{q}+\mathbf{G})\cdot\mathbf{r}} e^{-i\mathbf{G}\cdot\mathbf{c}} \Psi\left(\frac{|\mathbf{q}+\mathbf{G}|^2}{4\pi n_s}, \pi \eta^2\right) \\ & + \sqrt{n_s} \sum_{\mathbf{R}} e^{-i\mathbf{q}\cdot(\mathbf{R}-\mathbf{c})} \Phi\left(\pi \left[n_s |\mathbf{r} - \mathbf{R} + \mathbf{c}|^2 + \eta^2\right]\right). \end{aligned} \quad (13)$$

The functions  $\Phi(x)$  and  $\Psi(x, y)$ , defined in Appendix A, decay exponentially to zero for large  $x$ ; therefore,  $T_0$  and  $T_I$  contain only rapidly convergent sums.

The  $G = 0$  term in the first sum on the rhs of (12) and (13) give rise to a divergent term in  $E_0$  and in  $E_I$ , ensuing from the lack of charge neutrality. These terms are balanced by the interaction with a positive background, independently from the lattice geometry. Since the origin of the energy can be chosen arbitrarily, the divergent terms can be separated out and neglected in the calculation of the energy. This is done in Appendix B and the final result is

$$E_0 = 2e^2 \sqrt{n_s} \left\{ \sum_{\mathbf{R} \neq 0} \Phi\left(\pi n_s R^2\right) - 2 \right\}, \quad (14)$$

$$\begin{aligned} E_I = & e^2 \sqrt{n_s} \left\{ \sum_{\mathbf{R}} \Phi\left(\pi \left[n_s |\mathbf{R} + \mathbf{c}|^2 + \eta^2\right]\right) \right. \\ & \left. + \sum_{\mathbf{G} \neq 0} e^{i\mathbf{G}\cdot\mathbf{c}} \Psi\left(\frac{G^2}{4\pi n_s}, \pi \eta^2\right) + 2 \left\{ \pi \eta \operatorname{erfc} \sqrt{\pi} \eta - e^{-\pi \eta^2} \right\} \right\}, \end{aligned} \quad (15)$$

where  $G = |\mathbf{G}|$  and  $\operatorname{erfc}(x)$  is the complementary error function defined in Appendix A.

We have calculated  $E/e^2 \sqrt{n}$  (recall that  $n = 2n_s$ ) for the five different lattices listed in Table I. Phases I, III, and V are “rigid”, meaning that, for a fixed density, the cell is uniquely determined. On the contrary, phases II and IV are “soft”, because each of them contains a parameter, the ratio  $a_2/a_1$  of the length of the primitive vectors (aspect ratio) and

the angle between them, respectively, which can take on continuous values; at each value of  $\eta$ , this parameter is determined by energy minimization.

Figure 1 shows the calculated energy per particle of phases I, III, and V as a function of  $\eta$ ; the energy of phases II and IV would be nearly indistinguishable on the scale of this figure and will be shown later in Fig. 2. As we discussed in the introduction, phase I is energetically favoured at very small  $\eta$ , and it reduces to the SLWC at  $\eta = 0$ . At  $\eta = 0$  we find  $E = -1.96052 e^2 \sqrt{n}$ , which coincides with Ref. 19. At the opposite limit of large  $\eta$  the two sub-lattices become less and less coupled and the favoured geometry is composed of two staggered SLWC (phase V). Accordingly, the energy converges to the value  $E_0 = -1.96052 e^2 \sqrt{n}/\sqrt{2}$ , where the factor  $\sqrt{2}$  accounts for the reduced charge density. In the intermediate range of  $\eta$  the energetically favoured structure is phase III. The geometry of the three phases is sketched in the insets of Fig. 1, close to the range where they have the lowest energy.

Within the regions delimited by the open dots in Fig. 1, the energetically favoured structures are phases II and IV. These intermediate phases allow the lattice to pass from phase I to phase III, and from phase III to phase V, respectively. Note that phase II contains phase I and phase III as limiting cases, corresponding to the aspect ratios  $a_2/a_1 = \sqrt{3}$  and  $a_2/a_1 = 1$ , respectively. Analogously, phase IV contains phase III as limiting case for  $\theta = \pi/2$ . Therefore, the transitions I $\rightarrow$ II, II $\rightarrow$ III, and III $\rightarrow$ IV are continuous. Note, on the other hand, that there is no continuous way to pass from phase IV to phase V and, therefore, the transition IV $\rightarrow$ V is of the first order, i.e.,  $\partial E/\partial \eta$  exhibits a jump. Apparently, this point has been overlooked in Ref. 12, where the authors claim that the transition IV $\rightarrow$ V is continuous. The necessity for a first order phase transition when going from phase III to phase V has also been discussed, by use of general group theoretical arguments, by V. Fal'ko in Ref. 11.

Figure 2(a) shows the transition I $\rightarrow$ II $\rightarrow$ III on an enlarged scale. Phase I is energetically favoured only in a very small range around  $\eta = 0$ . As  $\eta > 0.006$ , in fact, a rectangular unit cell with  $a_2/a_1 < \sqrt{3}$  (phase II) is energetically favoured. In the inset of Fig. 2(a) we show how the aspect ratio  $a_2/a_1$  evolves in a continuous way during the transition; phase I evolves into phase III through an anisotropic shrinking of the rectangular unit cell, and eventually  $a_2/a_1 = 1$ , corresponding to phase III, is reached at  $\eta = 0.262$ .

The energy of phase IV is compared in Fig. 2(b) with the energy of phase III and V. For  $0.622 < \eta < 0.732$  the staggered rhombic lattice (phase IV) has the lowest energy. As shown in the inset, increasing  $\eta$  the angle  $\theta$  between the cell axes evolves continuously from  $90^\circ$ , corresponding to the square lattice (phase III), to  $69.48^\circ$ , and suddenly drops to  $60^\circ$ , which corresponds to phase V. The phase boundaries found above agree well with those found in Refs. 11 and 12.

To conclude this section, we give the asymptotic expressions of the static energy, for small and large  $\eta$ ,

$$\frac{E}{e^2 \sqrt{n}} = -1.96052 + \frac{1}{2\sqrt{2}} \left[ 2\pi\eta - 0.600434 \eta^2 + 2.86713 \eta^4 \right] \quad \text{for small } \eta, \quad (16)$$

$$\frac{E}{e^2 \sqrt{n}} = -\frac{1.96052}{\sqrt{2}} - \frac{v}{2\sqrt{2}} e^{-w\eta} \quad \text{for large } \eta, \quad (17)$$

where  $v = -3(\sqrt{3}/2)^{1/2}$  and  $w = (8\pi^2/\sqrt{3})^{1/2}$  in (17). Eqs. (16) and (17) reproduce the

correct energy within 2% for  $\eta < 0.3$  and within 0.2% for  $\eta > 0.5$ , respectively. We stress that the above expressions are not fitting functions, but have been obtained by a series expansion of (15) with respect to  $\eta$  in the relevant range. In Eq. (16) the linear term, ensuing from the last term in Eq. (15), is the only odd order term in the Taylor expansion and all higher order terms are even; the coefficients involve sums over the direct and the reciprocal lattice, which have been calculated numerically for the lattice of phase I. The coefficients in Eq. (17) can be obtained analytically, once one realizes that, for large  $\eta$ , only the first shell of  $\mathbf{G}$ 's needs to be retained in (15); higher order terms are proportional to  $e^{-\pi\eta^2}$  and decay faster for large  $\eta$ . In Ref. 12 two fitting expressions for the classical energy were given; however, we found that none of them have the correct limiting behaviour.

## II. DYNAMICAL PROPERTIES

In this section we calculate the frequencies of the phonon excitations of the five different phases within the harmonic approximation.

For a general lattice, the square of the phonon frequencies are the eigenvalues of the dynamical matrix defined by<sup>21</sup>

$$[\mathbf{T}(\mathbf{q}; l\kappa, l'\kappa')]_{\alpha\beta} = \frac{1}{(m_\kappa m_{\kappa'})^{1/2}} \sum_{l'} \phi_{\alpha\beta}(l\kappa, l'\kappa') e^{-i\mathbf{q}\cdot(\mathbf{R}_{l\kappa} - \mathbf{R}_{l'\kappa'})}, \quad (18)$$

where  $\mathbf{R}_{l\kappa}$  is the position vector of the  $\kappa$ -th particle in the  $l$ -th cell of the crystal, and  $m_\kappa$  its mass. The quantities  $\phi(l\kappa, l'\kappa')$  are the force constants defined by

$$\phi_{\alpha\beta}(l\kappa, l'\kappa') = \partial_\alpha \partial_\beta \phi(\mathbf{R}_{l\kappa} - \mathbf{R}_{l'\kappa'}), \quad (19)$$

where  $\phi(\mathbf{R}_{l\kappa} - \mathbf{R}_{l'\kappa'})$  is the two-body inter-particle potential. Here and in the following we use the notation  $\partial_\alpha F(\mathbf{x}) = \partial F(\mathbf{x}')/\partial x'_\alpha|_{\mathbf{x}=\mathbf{x}'}$ , where  $x_\alpha$  is the  $\alpha$ -th component of the vector  $\mathbf{x}$ . Due to translational invariance, the force constants satisfy the sum rule<sup>21</sup>

$$\sum_{l\kappa, l'\kappa'} \phi_{\alpha\beta}(l\kappa, l'\kappa') = 0. \quad (20)$$

Since each 2D unit cell of the BLWC contains two electrons, the dynamical matrix is a  $4 \times 4$  matrix which we write in block form as

$$\mathbf{D} = \begin{pmatrix} \mathbf{D}^{AA} & \mathbf{D}^{AB} \\ \mathbf{D}^{BA} & \mathbf{D}^{BB} \end{pmatrix}, \quad (21)$$

where  $\mathbf{D}^{AA}$ ,  $\mathbf{D}^{AB}$ ,  $\mathbf{D}^{BA}$ , and  $\mathbf{D}^{BB}$  are  $2 \times 2$  matrices. Applying (18) to the BLWC and using translational invariance, we obtain the matrix elements of  $\mathbf{D}^{AA}$  and  $\mathbf{D}^{AB}$

$$[\mathbf{D}^{AA}(\mathbf{q})]_{\alpha\beta} = \frac{1}{m_e} \sum_{\mathbf{R}} \phi_{\alpha\beta}(\mathbf{R}) e^{-i\mathbf{q}\cdot\mathbf{R}}, \quad (22)$$

$$[\mathbf{D}^{AB}(\mathbf{q})]_{\alpha\beta} = \frac{1}{m_e} \sum_{\mathbf{R}} \phi_{\alpha\beta}(\mathbf{R} - \mathbf{c}) e^{-i\mathbf{q}\cdot(\mathbf{R} - \mathbf{c})}, \quad (23)$$

where  $m_e$  is the electron mass, and the force constants are

$$\phi_{\alpha\beta}(\mathbf{R}) = \partial_\alpha \partial_\beta \frac{e^2}{R}, \quad \mathbf{R} \neq 0, \quad (24)$$

and

$$\phi_{\alpha\beta}(\mathbf{R} - \mathbf{c}) = \partial_\alpha \partial_\beta \frac{e^2}{\left[|\mathbf{R} - \mathbf{c}|^2 + d^2\right]^{1/2}}. \quad (25)$$

Using Eq. (20), we find the force constant for  $\mathbf{R} = 0$

$$\phi_{\alpha\beta}(\mathbf{R} = 0) = - \left[ \sum_{\mathbf{R} \neq 0} \phi_{\alpha\beta}(\mathbf{R}) + \sum_{\mathbf{R}} \phi_{\alpha\beta}(\mathbf{R} - \mathbf{c}) \right]. \quad (26)$$

Furthermore, since the two sub-lattices are equivalent, we have  $\mathbf{D}^{AA} = \mathbf{D}^{BB}$  and, using Eq. (18),  $\mathbf{D}^{AB} = [\mathbf{D}^{BA}]^\dagger$ .

It turns out to be convenient to define

$$[\mathbf{S}^{AA}(\mathbf{q})]_{\alpha\beta} = -e^2 \sum_{\mathbf{R} \neq 0} \partial_\alpha \partial_\beta \frac{e^{-i\mathbf{q} \cdot \mathbf{R}}}{R}, \quad (27)$$

$$[\mathbf{S}^{AB}(\mathbf{q})]_{\alpha\beta} = -e^2 \sum_{\mathbf{R}} \partial_\alpha \partial_\beta \frac{e^{-i\mathbf{q} \cdot (\mathbf{R} - \mathbf{c})}}{\left[|\mathbf{R} - \mathbf{c}|^2 + d^2\right]^{1/2}}, \quad (28)$$

which can be obtained from  $T_0$  and  $T_I$

$$[\mathbf{S}^{AA}(\mathbf{q})]_{\alpha\beta} = -e^2 \lim_{r \rightarrow 0} \partial_\alpha \partial_\beta T_0(\mathbf{r}, \mathbf{q}), \quad (29)$$

$$[\mathbf{S}_{AB}(\mathbf{q})]_{\alpha\beta} = -e^2 \partial_\alpha \partial_\beta T_I(0, \mathbf{q}). \quad (30)$$

Then the matrix elements of the dynamical matrix can be written

$$\mathbf{D}^{AA}(\mathbf{q}) = \frac{1}{m_e} [\mathbf{S}^{AA}(0) + \mathbf{S}^{AB}(0) - \mathbf{S}^{AA}(\mathbf{q})], \quad (31)$$

$$\mathbf{D}^{AB}(\mathbf{q}) = \frac{1}{m_e} [-\mathbf{S}^{AB}(\mathbf{q})]. \quad (32)$$

Using the rapidly convergent form for  $T_0$  and  $T_I$ , as given in (12) and (13), allows one to write down the matrix elements of  $\mathbf{S}^{AA}$  and  $\mathbf{S}^{AB}$  explicitly

$$\begin{aligned} [\mathbf{S}^{AA}(\mathbf{q})]_{\alpha\beta} = \sqrt{n_s} \left\{ - \sum_{\mathbf{G}} (\mathbf{q} + \mathbf{G})_\alpha (\mathbf{q} + \mathbf{G})_\beta \Phi \left( \frac{|\mathbf{q} + \mathbf{G}|^2}{4\pi n_s} \right) \right. \\ \left. + \sum_{\mathbf{R} \neq 0} \bar{V}_{\alpha\beta}(\pi n_s R^2) e^{-i\mathbf{q} \cdot \mathbf{R}} + \delta_{\alpha\beta} \frac{4}{3}(\pi n_s) \right\}, \end{aligned} \quad (33)$$

$$\begin{aligned} [\mathbf{S}^{AB}(\mathbf{q})]_{\alpha\beta} = \sqrt{n_s} \left\{ - \sum_{\mathbf{G}} (\mathbf{q} + \mathbf{G})_\alpha (\mathbf{q} + \mathbf{G})_\beta \Psi \left( \frac{|\mathbf{q} + \mathbf{G}|^2}{4\pi n_s}, \pi \eta^2 \right) e^{-i\mathbf{G} \cdot \mathbf{c}} \right. \\ \left. + \sum_{\mathbf{R}} \bar{V}_{\alpha\beta}(\pi n_s |\mathbf{R} - \mathbf{c}|^2) e^{-i\mathbf{q} \cdot (\mathbf{R} - \mathbf{c})} \right\}, \end{aligned} \quad (34)$$



where we have defined

$$\overline{V}_{\alpha\beta}(X^2) = \partial_\alpha \partial_\beta \Phi(X^2) = 2\pi n_s \left\{ \delta_{\alpha\beta} \Phi'(X^2) + 2\pi n_s X_\alpha X_\beta \Phi''(X^2) \right\}. \quad (35)$$

In general  $\mathbf{D}$  is a complex hermitian matrix. However, since in the BLWC the two sites of each cell are occupied by identical particles, it is possible to apply a unitary transformation which results in a real symmetric matrix.<sup>22</sup> If we denote with  $\mathbf{I}_2$  the  $2 \times 2$  identity matrix, the transformation

$$\mathbf{U} = \frac{1}{\sqrt{2}} \begin{pmatrix} \mathbf{I}_2 & i\mathbf{I}_2 \\ i\mathbf{I}_2 & \mathbf{I}_2 \end{pmatrix} \quad (36)$$

results in

$$\overline{\mathbf{D}} = \mathbf{U} \mathbf{D} \mathbf{U}^{-1} = \begin{pmatrix} \mathbf{D}_{AA} + \text{Im } \mathbf{D}_{AB} & \text{Re } \mathbf{D}_{AB} \\ \text{Re } \mathbf{D}_{AB} & \mathbf{D}_{AA} - \text{Im } \mathbf{D}_{AB} \end{pmatrix}, \quad (37)$$

where  $\text{Re } \mathbf{D}_{AB}$  and  $\text{Im } \mathbf{D}_{AB}$  are the real and imaginary parts of  $\mathbf{D}_{AB}$ . Note that  $\text{Im } \mathbf{D}_{AB} = 0$  for a lattice with inversion symmetry. This applies to all phases, except for phase V.

Finally, we solved the set of four linear equations

$$\left( \overline{\mathbf{D}}(\mathbf{q}) - \omega_{\mathbf{q},j}^2 \mathbf{I}_4 \right) \mathbf{e}(\mathbf{q}, j) = 0, \quad (38)$$

where  $\mathbf{I}_4$  is the  $4 \times 4$  identity matrix,  $\omega_{\mathbf{q},j}$  is the frequency of the  $j$ -th phonon mode ( $j = 1, \dots, 4$ ) with wavevector  $\mathbf{q}$ , and  $\mathbf{e}(\mathbf{q}, j)$  its eigenvector. Equation (38) is equivalent to the diagonalization of the  $4 \times 4$  matrix  $\overline{\mathbf{D}}$ , which provides the four eigenvalues  $\omega_{\mathbf{q},j}^2$  at each point  $\mathbf{q}$  in reciprocal space. For a lattice to be stable, it is necessary that  $\omega_{\mathbf{q},j}^2 > 0$ .

Figure 3 shows the frequencies  $\omega_{\mathbf{q},j}$  (or, when  $\omega_{\mathbf{q},j}^2$  is negative, its imaginary part) for phases: (a) I, (b) III, and (c) V, and their evolution with  $\eta$ . Frequencies are given in terms of the characteristic frequency  $\omega_1 = e^2 n^{3/2} / m_e$ , which depends on the density and not on the lattice geometry. Phonon dispersions are shown along the high symmetry directions in reciprocal space. The high symmetry points are labeled according to the insets. We recall that in a SLWC the transverse acoustical (TA) and the longitudinal acoustical (LA) modes vanish at the  $\Gamma$  point as  $q$  and  $q^{1/2}$ , respectively.<sup>19</sup> Thus the sound velocity of the LA mode is infinite. The latter behaviour is a general property of a 2D Coulomb plasma<sup>19</sup> and does not depend on the lattice geometry, nor on  $d$ , as is clear from a comparison of the three panels in Fig. 3. The remaining two (optical) modes ensuing from (38) are peculiar to the BLWC and correspond to out-of-phase vibrations of electrons in opposite layers.

Starting from the top panel, it is shown in Fig. 3 that, as  $\eta$  is increased, the TA mode of phase I softens until, above a critical value of  $\eta$ , the frequency becomes imaginary, indicating a lattice instability. For  $\eta$  between 0.262 and 0.622 phase III (square lattice) is energetically favoured, according to Fig. 2. We recall that in a SLWC the square lattice cannot exist, since it has an imaginary TA branch.<sup>19</sup> Figure 3(b) shows, on the other hand, that in the BLWC the square lattice is stable for a certain range of  $\eta$ . For  $\eta$  below a critical value, however, the TA branch softens along the  $\Gamma M$  direction and eventually becomes imaginary, as is expected from the fact that in this limit the BLWC tends to the SLWC; at the opposite

limit of large  $\eta$ , the TA branch softens along the  $\Gamma X$  direction and eventually phase III becomes unstable, as the BLWC tends to two separated SLWC's.

Phase V is stable for large  $\eta$  [Fig. 3(c)]. In the limit  $\eta \rightarrow \infty$  we have the phonon dispersion curves of two uncoupled SLWCs; therefore, in Fig. 3, each curve in the  $\eta = \infty$  case is doubly degenerate and all modes approach zero for  $q \rightarrow 0$ . For smaller  $\eta$ , optical modes with a finite frequency at the  $\Gamma$  point appear; at the same time, the TA mode becomes softer and, eventually, becomes imaginary at  $\eta \sim 0.6$ .

The sound velocity of the TA mode,  $v_{TA} = d\omega_{TA}/dq|_{q=0}$ , along the in-plane directions  $(1, 0)$  and  $(1, 1)$ , and for the five phases, is shown in detail in Fig. 4. The labels on top of the figure indicate the energetically favoured phase in each range of  $\eta$ , according to Figs. 1 and 2; phase I is favoured only in a very small range around  $\eta = 0$  and, therefore, is not indicated. The vanishing of the low-frequency modes in certain directions, shown in Fig. 4, sets a limit to the range of stability of each phase. Note that phases II and III have a soft mode at a value of  $\eta$  which coincides with the value where the transition between the two phases takes place (the vertical dotted line). The same happens for phases III and IV. Therefore, the range where phase III is energetically favoured coincides with the range of stability of this phase. This has profound implications in determining the DLWC phase diagram at  $T \neq 0$ , as we will show in the next section. Note also that in the range of  $\eta$  where phase II is energetically favoured, both phases I and II are stable, i.e., they do not have imaginary phonon frequencies. Analogously, in the range where phase IV is energetically favoured, both phases IV and V are stable. The  $T=0$  phase diagram, deduced from Figs. 1 and 2, and the range of stability, deduced from the softening of phonon modes, are summarized in Fig. 5.

Figure 6 shows the evolution of the optical frequencies at the  $\Gamma$  point,  $\omega_{opt}$ , with  $\eta$ . For phases III and V the two optical frequencies are degenerate. It has been noted that the detection of the exponential decay of the optical modes at large  $\eta$  could serve as a fingerprint of the solid phase in a bi-layer structure.<sup>11</sup> Note also the different behaviour of the optical modes between phase I and II, and between IV and V, which may be used experimentally to distinguish between the different possible phases.

The dependence of the sound velocity and of the optical modes at the  $\Gamma$  point upon  $\eta$  has been fitted to simple analytical expressions in the low  $\eta$  (below  $\sim 0.2$ ) and in the large  $\eta$  (above  $\sim 0.7$ ) range. The sound velocity  $v_{TA}$  (see Fig. 4) has been fitted to

$$v_{TA}\sqrt{n}/\omega_1 = p_0 + p_2\eta^2 + p_4\eta^4 \quad (39)$$

for small  $\eta$ , and to

$$v_{TA}\sqrt{n}/\omega_1 = p_0 + p_2\eta^{-2} + p_4\eta^{-4} \quad (40)$$

for large  $\eta$ . The coefficients  $p_i$  for phases I, II (small  $\eta$ ) and V (large  $\eta$ ) are reported in Table II. The frequencies  $\omega_{opt}$  (see Fig. 6) have been fitted to

$$\omega_{opt}/\omega_1 = q_0 + q_2\eta^2 + q_4\eta^4 \quad (41)$$

for small  $\eta$ , and to

$$\omega_{opt}/\omega_1 = q_1 e^{-q_2\eta} \quad (42)$$

for large  $\eta$ . For  $\eta \sim 0.262$ , close to the boundary between phase II and phase III, the optical modes of phase II have a singular behaviour. In this range we have fitted  $\omega_{opt}$  to

$$\omega_{opt}/\omega_1 = q_0 + q_1(q_2 - \eta)^{q_3}. \quad (43)$$

The coefficients  $q_i$  are reported in Table III. The agreement with the full calculations did not improve by adding odd powers of  $\eta$  in Eqs. (39), (40), and (41). All the above fitting functions give the correct values with an accuracy better than 0.6 % in the relevant ranges of  $\eta$ .

In Fig. 7 we report the evolution with  $\eta$  of the phonon density of state (DOS). At each value of  $\eta$ , we show the DOS of the phase which is energetically favoured at that value. At  $\eta = 0$  and  $\eta = \infty$  the energetically favoured lattice are, respectively, the SLWC lattice with density  $n$  (phase I), and two uncoupled SLWCs with density  $n/2$  (phase V); therefore, the corresponding DOS curves are equal up to a factor  $2^{3/4}$  in the frequency scale. Note in Fig. 7 the peak of optical frequencies which narrows at  $\eta \sim 0.5$ , corresponding to the range of  $\eta$  where the in-plane component of the average interaction of one particle with its NN's in the same layer and in the opposite layer are similar. Also note the low-frequency peak which moves to very low frequencies around  $\eta \sim 0.3$  and  $\eta \sim 0.7$ . This behaviour is reminiscent of the softening of the TA mode of the square lattice (phase III) discussed above. The resulting high density of low-frequency modes suggests that very large fluctuations of particles around their equilibrium lattice sites are possible; correspondingly, a low melting temperature is expected in proximity of these points, as will be discussed in Sec. III.

### III. PHASE DIAGRAM AND MELTING

In this section we will be concerned with the non-zero temperature properties of the BLWC. First, we will use the calculated phonon excitation frequencies to estimate the melting temperature  $T_M$  via the Lindemann criterion. In principle, only order of magnitude estimates of  $T_M$  are expected from an harmonic theory, since anharmonic terms of the potential become important when crystal vibrations are so large that the lattice is near to dissolve. In the case of the SLWC, apart from simulations, analytical methods have been successfully used to calculate  $T_M$  by including anharmonic effects.<sup>20,23</sup> These methods assume that melting proceeds through the dislocation mediated mechanism proposed by Kosterlitz and Thouless,<sup>6</sup> Halperin and Nelson,<sup>7</sup> and Young<sup>8</sup> (KTHNY theory). The ingredient of these calculations is the sound velocity of the TA mode of the lattice, which is assumed isotropic in the KTHNY theory and which is indeed the case in the simple hexagonal lattice of the SLWC, but not in the BLWC, where the TA mode, in general, is anisotropic, as is clear from Fig. 4. Therefore, in this work we will rely on the simple Lindemann criterion. We shall see that, taking the Lindemann parameter  $\delta$ , defined in Eq. (44) below, from existing simulations, effectively includes anharmonic effects into the theory to some extent.

The Lindemann criterion states that, in a lattice of density  $n$ , melting occurs when

$$\frac{\langle u^2 \rangle}{r_0^2} = \delta^2, \quad (44)$$

i.e., when the mean square displacement of a lattice site around its equilibrium position  $\langle u^2 \rangle$  exceeds a certain fraction of the mean inter-particle distance  $r_0 = 1/\sqrt{\pi n}$ . The brackets  $\langle \dots \rangle$  represent the thermodynamic average; in our case the latter will be calculated within the harmonic theory. The parameter  $\delta$  is an input to the criterion, to be obtained from simulations or from some analytic theory. Equation (44) has been verified in simulations of several 3D systems.<sup>24</sup> It is known, however, that  $\langle u^2 \rangle$  is logarithmically divergent in 2D. On the other hand, the *relative* mean square displacement  $\langle |\mathbf{u}(\mathbf{R}) - \mathbf{u}(\mathbf{R} + \mathbf{a})|^2 \rangle$ , where  $\mathbf{u}(\mathbf{R})$  and  $\mathbf{u}(\mathbf{R} + \mathbf{a})$  are the displacement vectors at lattice site  $\mathbf{R}$  and at the NN site  $\mathbf{R} + \mathbf{a}$ , where  $\mathbf{a}$  is the vector joining two NN's, is finite. Correspondingly, a *modified* Lindemann criterion can be defined

$$\frac{\langle |\mathbf{u}(\mathbf{R}) - \mathbf{u}(\mathbf{R} + \mathbf{a})|^2 \rangle}{r_0^2} = \delta_m^2. \quad (45)$$

The value of  $\delta_m^2$  at melting has been calculated in simulations of melting in a SLWC and turned out to be  $\simeq 0.1$ .<sup>18</sup> In principle,  $\delta_m$  may depend on the lattice geometry and the nature of the interaction; however, the Lindemann parameter has been found to be quite independent from the form of the interaction both in 2D<sup>18</sup> and in 3D<sup>24</sup> systems; therefore, we take  $\delta_m^2 = 0.1$ , and independent from  $\eta$  and from the lattice geometry. Small variations of  $\delta_m$  would not change our results qualitatively.

The correlation function  $\langle |\mathbf{u}(\mathbf{R}) - \mathbf{u}(\mathbf{R} + \mathbf{a})|^2 \rangle$  is calculated within the harmonic theory.<sup>21</sup> Each lattice site in the BLWC has two types of NN's, in general at a different distance, and the number and distance of the NN's changes in a continuous way with  $\eta$ . Accordingly, we calculate separately two (in general different) correlation functions

$$\begin{aligned} L_1 &= \frac{1}{M_1} \sum_{\alpha=x,y} \sum_{m=1 \dots M_1} \langle |u_\alpha^A(0) - u_\alpha^A(m)|^2 \rangle \\ &= \frac{4k_B T}{Nm_e M_1} \sum_{\mathbf{q}j} \frac{[e_x^A(\mathbf{q}, j)]^2 + [e_y^A(\mathbf{q}, j)]^2}{\omega_{\mathbf{q},j}^2} \sum_{m=1 \dots M_1} \sin^2 \frac{\mathbf{q} \cdot \mathbf{R}_m}{2}, \end{aligned} \quad (46)$$

$$\begin{aligned} L_2 &= \frac{1}{M_2} \sum_{\alpha=x,y} \sum_{m=1 \dots M_2} \langle |u_\alpha^A(0) - u_\alpha^B(m)|^2 \rangle \\ &= \frac{k_B T}{Nm_e M_2} \sum_{\mathbf{q}j} \frac{1}{\omega^2(\mathbf{q}, j)} \sum_{m=1 \dots M_1} \left\{ 1 - 2 \left[ e_x^A(\mathbf{q}, j) e_x^B(\mathbf{q}, j) + e_y^A(\mathbf{q}, j) e_y^B(\mathbf{q}, j) \right] \cos \mathbf{q} \cdot \mathbf{R}_m \right\}, \end{aligned} \quad (47)$$

where  $k_B$  is the Boltzmann constant,  $u_\alpha^{A(B)}$  is the  $\alpha$ -th component of the displacement vector in layer A(B) calculated at the origin (0) or at the position of the  $m$ -th NN.  $e_\alpha^{A(B)}(\mathbf{q}, j)$  is the  $\alpha$ -th component of the eigenvector of the  $j$ -th mode, at point  $\mathbf{q}$ , relative to the sub-lattice in layer A(B),  $\mathbf{R}_m$  is the relative lattice vector connecting one site to its  $m$ -th NN in the same ( $L_1$ ) or in the opposite ( $L_2$ ) layer, and the sums over  $m$  are extended to the  $M_1$  ( $M_2$ ) NN's in the same (opposite) sub-lattice.

Now we consider two limiting cases. For  $\eta = 0$ ,  $\langle |\mathbf{u}(\mathbf{R}) - \mathbf{u}(\mathbf{R} + \mathbf{a})|^2 \rangle = L_1 + L_2$ , since all NN's are equivalent. At the opposite limit,  $\eta \rightarrow \infty$ ,  $\langle |\mathbf{u}(\mathbf{R}) - \mathbf{u}(\mathbf{R} + \mathbf{a})|^2 \rangle = L_1$ , since the dynamics in one layer is not influenced by the sub-lattice on the opposite layers. Therefore, we write in general

$$\langle |\mathbf{u}(\mathbf{R}) - \mathbf{u}(\mathbf{R} + \mathbf{a})|^2 \rangle = L_1 + f(\eta)L_2, \quad (48)$$

where the function  $f(\eta)$  satisfies

$$f(0) = 1, \quad f(\infty) = 0. \quad (49)$$

As  $f(\eta)$  represents the influence of the oscillation in one layer on the oscillations in the opposite layer, we take  $f(\eta)$  proportional to the in-plane component of the Coulombic force between two NN sites sitting in opposite layers. This is

$$F_{\parallel}(d) = -\frac{e^2 c}{(c^2 + d^2)^{3/2}} \quad (50)$$

where  $c = |\mathbf{c}|$ . Taking  $f(\eta)$  proportional to  $F_{\parallel}(d)$ , and imposing the conditions (49), we have

$$f(\eta) = \frac{1}{(1 + \alpha_p \eta^2)^{3/2}}, \quad (51)$$

where  $\alpha_p = (nc^2)^{-1}$  is a dimensionless geometric factor which can be calculated from Table I.

Inserting Eq. (48) in (45) and using  $r_0^2 = 1/\pi n_s$ , we have calculated the melting temperature  $T_M$ , which is reported in Fig. 8 for the five phases. For the “soft” phases II and IV,  $T_M$  was calculated taking the  $T = 0$  value of the aspect ratio and  $\theta$ , respectively. This will be justified later.

In the studies of melting of the SLWC, the melting temperature is usually given in terms of the dimensionless parameter  $\Gamma_M = e^2 \sqrt{\pi n} / K T_M$  (the inverse of the vertical units in Fig. 8), the ratio between the average Coulombic potential energy and the average kinetic energy. Experiments<sup>2</sup> give  $\Gamma_M \simeq 131$  and simulations<sup>25</sup> give  $\Gamma_M \simeq 128$ . Using the harmonic value of the sound velocity at  $T = 0$ , the KTHNY theory gives  $\Gamma_M \simeq 79$ . Our calculation, which is performed within the harmonic approximation, but uses  $\delta_m$  taken from simulations which, of course, include anharmonic effects, gives  $k_B T_M / e^2 \sqrt{\pi n} = 0.00925$  at  $\eta = 0$ , corresponding to  $\Gamma_M = 108$ . Therefore, our calculation, although overestimates  $T_M$ , partially includes anharmonic effects. In a full anharmonic theory,  $L_1$  and  $L_2$ , which in the harmonic approximation scale linearly with  $T$ , would increase more rapidly, especially close to the melting transition.

Fig. 8 shows that the melting temperature has an oscillating behaviour as a function of  $\eta$ . This is a consequence of the vanishing of the TA phonon modes at the phase boundaries II/III and III/IV, as discussed in Sec. II. Therefore, for fixed  $T \neq 0$  and as function of  $\eta$  we observe that alternating solid and liquid phases are possible, and the reentrant solid phase has a different lattice geometry each time. Furthermore, note from the inset of Fig. 8 that, for large values of  $\eta$ ,  $T_M$  approaches the melting temperature of a SLWC of density  $n/2$  from below. In certain experimental realizations of the BLWC it could be easier to change  $\eta$  through a change in the charge density, keeping  $d$  constant. Therefore, in Fig. 9 we show the calculated melting temperature in units of  $k_B T_M d / e^2 \sqrt{\pi}$ . Note that in the classical regime the phase diagram is determined by  $\eta$  and a dimensionless temperature, either  $k_B T_M / e^2 \sqrt{\pi n}$  or  $k_B T_M d / e^2 \sqrt{\pi}$ . In the quantum regime, instead, the kinetic energy term depends on the density alone and, therefore, the phase diagram must be drawn explicitly in the three-parameter space  $(d, n, T)$ .

The presence of different lattice geometries which are stable within the same range of  $\eta$  suggests the possibility that, increasing  $T$  at fixed  $\eta$ , the BLWC undergoes a structural phase transition, and, eventually, melts at a temperature appropriate to the high temperature phase. For example, it seems possible that for  $\eta < 0.262$  the BLWC evolves from phase II (with some value of the aspect ratio which minimizes the static energy at  $T = 0$ ) to phase I (aspect ratio  $\sqrt{3}$ ), as  $T$  exceeds some critical value, and eventually melts at a  $T_M$  appropriate for phase I. To investigate such possibility we have minimized the free energy with respect to the lattice geometry at fixed  $\eta$  and  $T$ . The harmonic approximation of the free-energy in the high-temperature limit is

$$F(\xi) = E(\xi) + k_B T \sum_{\mathbf{q}, j} \log \frac{\hbar \omega_{\mathbf{q}, j}(\xi)}{k_B T}, \quad (52)$$

where  $\xi$  is a parameter which defines a distortion of the lattice. There are two ranges of  $\eta$  where more than one phase is stable with respect to lattice vibrations (see Figs. 4 and 5); in the range  $0.006 < \eta < 0.262$  phase II is energetically favoured, but also phase I is stable throughout this range. Therefore, in this range, we minimize  $F$  with respect to  $\xi = a_2/a_1$ . In the range  $0.622 < \eta < 0.732$  phase IV is energetically favoured, but also phase V is stable; therefore, in this range we take  $\xi = \theta$ . Integration over reciprocal space in (52) was performed numerically. We found that in both ranges the value of  $\xi$  which minimizes  $F$  is practically independent of the temperature and, therefore, coincides with the  $T = 0$  value. In other words, the phase boundaries between the different geometries in Fig. 8 are represented by vertical lines. Moreover, this justifies the fact that, in order to calculate  $T_M$  for the “soft” phases II and IV, we have used the  $T = 0$  value for the aspect ratio and  $\theta$ , respectively.

## CONCLUSIONS

The phase diagram of a classical BLWC, both at  $T = 0$  and at  $T \neq 0$  was investigated, within an harmonic approach, by use of the Lindemann criterion and minimization of the harmonic free-energy. Five different crystalline geometries are stable in different ranges of inter-layer distance/charge densities. Moreover, at  $T = 0$  the five phases evolve one into the other through both continuous and discontinuous transitions. At  $T \neq 0$ , alternating solid and liquid phases are possible, as one sweeps the inter-layer distance or the charge density. In particular, regions of liquid phase separate phase II from phase III, and phase III from phase IV. This has been shown to be a consequence of lattice instabilities induced by the vanishing of phonon modes at the phase boundaries. On the other hand, a first order transition line separates IV from phase V.

An additional intricacy of the phase diagram in the small  $\eta$  range has been pointed out by Vil’k and Monarkha<sup>10</sup>. In this limit the hamiltonian (3) was mapped into the hamiltonian of a binary mixture of particles sitting on a triangular lattice and interacting through a dipole potential. Therefore there is a possibility that a disordered phase appears, as the temperature is increased. They find two phase transitions. The low temperature (ordered) phase is equivalent to our phase I. Above a critical temperature  $T_1$  the lattice can be seen as composed of three inter-penetrating triangular lattices, two of which are ordered and one

is disordered. Above a second critical temperature  $T_2$  the lattice becomes completely disordered. Of course the order-disorder transition vanishes as  $\eta \rightarrow 0$ , where the two sublattices become equivalent.

A bi-layer electron gas can easily be realized in semiconductor heterostructures.<sup>16,26</sup> Although our results have been obtained for a classical system, they can give some indications on the phase diagram in quantum bi-layer structures, provided that temperature fluctuations are interpreted as quantum fluctuations. Very recently, in Ref. 12 a re-entrant phase around  $\eta \simeq 2.6$ , analogous to ours in Fig. 8, was predicted in the  $(\eta, r_s)$  phase diagram, where  $r_s$  is the dimensionless inverse electron density. Furthermore, our analysis of the phonon excitations and the analytical fitting that we have developed retain their validity in the quantum regime.

In principle, the harmonic approximation used throughout this work is expected to fail when the temperature approaches the melting temperature. However, we have shown that, in the  $\eta = 0$  case, we obtain  $T_M$  in reasonable agreement with numerical simulations and experiments on the SLWC; therefore, we believe that inclusion of the anharmonic effects would not change our results qualitatively, as far as the melting temperature is concerned. We believe also that the approximation of a structure independent parameter  $\delta_m$  in the Lindemann criterion should not change the nature of our findings. The harmonic approach could be a more severe approximation in the calculation of the free-energy and our investigation, therefore, does not rule out completely the possibility of temperature-induced structural phase transitions.

## ACKNOWLEDGMENTS

We acknowledge financial support from the HCM network No. ERBCHRXCT930374, a NATO Collaborative Research Grant, and the Belgian National Science Foundation. Discussions with V. A. Schweigert, K. Michel, J. Naudts, I. Kono, M. Saitoh and Yu. P. Monarkha are gratefully acknowledged.

## APPENDIX A: RAPIDLY CONVERGENT FORM OF $T_0$ AND $T_I$

The slowly convergent sums over lattice sites appearing in the definition of  $T_0$  and  $T_I$  [Eqs. (8) and (9)] cannot be used in a numerical calculation. Therefore, they will be converted into a rapidly convergent form using a generalization of the Ewald method.<sup>20</sup> Formally, we proceed as follows. First, each term in the sum is decomposed in two terms, using the identity

$$\frac{1}{r} = \frac{1}{r} \{ \operatorname{erf}(\varepsilon r) + \operatorname{erfc}(\varepsilon r) \}, \quad (\text{A1})$$

where

$$\operatorname{erf}(x) = \frac{2}{\sqrt{\pi}} \int_0^x e^{-t^2} dt, \quad (\text{A2})$$

is the error function,  $\text{erfc}(x) = 1 - \text{erf}(x)$  is the complementary error function, and  $\varepsilon$  is an arbitrary constant. The reason why we do so, is that  $\text{erfc}(x)$  vanishes exponentially for large values of the argument and, consequently, the lattice sum with this function as argument is sufficiently rapidly convergent. Then, the other lattice sum with argument  $\text{erf}(x)$  is mapped onto a sum over the reciprocal lattice, using the 2D theta-function transformation.<sup>27</sup>

Using (A1) and the definition of  $T_0$  [Eq. (8)], we obtain

$$T_0 = e^{-i\mathbf{q}\cdot\mathbf{r}} \sum_{\mathbf{R}} \frac{e^{i\mathbf{q}\cdot(\mathbf{r}-\mathbf{R})}}{|\mathbf{r}-\mathbf{R}|} \text{erf}(\varepsilon |\mathbf{r}-\mathbf{R}|) + \sum_{\mathbf{R} \neq 0} \frac{e^{-i\mathbf{q}\cdot\mathbf{R}}}{|\mathbf{r}-\mathbf{R}|} \text{erfc}(\varepsilon |\mathbf{r}-\mathbf{R}|) + \frac{\text{erfc}(\varepsilon r)}{r} - \frac{1}{r}. \quad (\text{A3})$$

To convert the first sum on the rhs of (A3) into a rapidly convergent form, we substitute  $\xi = t/\lambda$  in the definition of the error function, which results into

$$\frac{\text{erf}(\varepsilon \lambda)}{\lambda} = \frac{2}{\sqrt{\pi}} \int_0^\varepsilon e^{-\lambda^2 \xi^2} d\xi. \quad (\text{A4})$$

with  $\lambda = |\mathbf{r}-\mathbf{R}|$ . We plug (A4) into the first sum of (A3) and we bring the sum under the integral. Next, we apply the 2D theta-function transformation<sup>27</sup>

$$\sum_{\mathbf{R}} e^{-|\mathbf{r}-\mathbf{R}|^2 \xi^2} e^{-i\mathbf{q}\cdot\mathbf{R}} = \frac{n_s \pi}{\xi^2} \sum_{\mathbf{G}} e^{-|\mathbf{q}+\mathbf{G}|^2 / 4\xi^2} e^{-i(\mathbf{q}+\mathbf{G})\cdot\mathbf{r}}, \quad (\text{A5})$$

and the substitution  $t = |\mathbf{q}+\mathbf{G}|/2\xi$ , which transforms the first term on the rhs of (A3) into

$$2\pi n_s \sum_{\mathbf{G}} e^{-i(\mathbf{q}+\mathbf{G})\cdot\mathbf{r}} \frac{\text{erfc}(|\mathbf{q}+\mathbf{G}|/2\varepsilon)}{|\mathbf{q}+\mathbf{G}|}. \quad (\text{A6})$$

The final step is to choose a reasonable value for  $\varepsilon$ , such that the lattice sums have a sufficient rapid numerical convergency. A convenient choice is  $\varepsilon = r_0^{-1} = \sqrt{\pi n_s}$ . Defining the function

$$\Phi(x) = \sqrt{\frac{\pi}{x}} \text{erfc}(\sqrt{x}) \quad (\text{A7})$$

to simplify the final expression, we finally obtain Eq. (12).

For  $T_I$  we proceed in a similar way. Let  $\lambda^2 = |\mathbf{r}-\mathbf{R}+\mathbf{c}|^2 + d^2$ ; using (A1), and the definition of  $T_I$  [Eq. (9)], we have

$$T_I = e^{-i\mathbf{q}\cdot\mathbf{r}} \sum_{\mathbf{R}} \frac{e^{i\mathbf{q}\cdot(\mathbf{r}-\mathbf{R}+\mathbf{c})}}{\lambda} [\text{erf}(\varepsilon \lambda) + \text{erfc}(\varepsilon \lambda)]. \quad (\text{A8})$$

Using the identity (A4), the 2D theta-function transformation (A5), and the substitution  $t = |\mathbf{q}+\mathbf{G}|/2\xi$ , the first term in (A8) becomes

$$\frac{4}{\sqrt{\pi}} \pi n_s \sum_{\mathbf{G}} \frac{e^{-i\mathbf{G}\cdot\mathbf{c}} e^{-i(\mathbf{q}+\mathbf{G})\cdot\mathbf{r}}}{|\mathbf{q}+\mathbf{G}|} \int_{|\mathbf{q}+\mathbf{G}|/2\varepsilon}^{\infty} e^{-d^2 |\mathbf{q}+\mathbf{G}|^2 / 4t^2} e^{-t^2} dt. \quad (\text{A9})$$



The integral can be performed analytically; using

$$\int_x^\infty e^{-(t^2+\alpha^2/t^2)} dt = \frac{\sqrt{\pi}}{4} \left[ e^{2\alpha} \operatorname{erfc} \left( x + \frac{\alpha}{x} \right) + e^{-2\alpha} \operatorname{erfc} \left( x - \frac{\alpha}{x} \right) \right], \quad (\text{A10})$$

inserting  $\varepsilon = \sqrt{\pi n_s}$ , and defining the function

$$\Psi(x, y) = \frac{1}{2} \sqrt{\frac{\pi}{x}} \left[ e^{\sqrt{4xy}} \operatorname{erfc}(\sqrt{x} + \sqrt{y}) + e^{-\sqrt{4xy}} \operatorname{erfc}(\sqrt{x} - \sqrt{y}) \right], \quad (\text{A11})$$

we finally obtain Eq. (13).

## APPENDIX B: EXPLICIT EXPRESSIONS FOR $E_0$ AND $E_I$

The energy  $E_0$ , calculated from Eq. (10), contains the divergent term

$$\begin{aligned} e^2 \sqrt{n_s} \Phi \left( \frac{G^2}{4\pi n_s} \right) \Big|_{G=0} &= e^2 \left[ \frac{2\pi n_s}{G} - \frac{2\pi n_s}{G} \operatorname{erf} \left( \frac{G}{2\sqrt{\pi n_s}} \right) \right] \Big|_{G=0} \\ &= e^2 n_s \frac{2\pi}{G} \Big|_{G=0} - 2e^2 \sqrt{n_s}, \end{aligned} \quad (\text{B1})$$

where we have made use of the limit

$$\lim_{x \rightarrow 0} x^{-1} \operatorname{erf}(x) = 2/\sqrt{\pi}. \quad (\text{B2})$$

in the second line of (B1). The divergent term in the last line of (B1) is independent of the lattice geometry and can be neglected. In fact the divergency is exactly balanced by the interaction energy of the electrons with a positive background located in the same layer<sup>19</sup>

$$E_0^b = -e^2 n_s \int \frac{d\mathbf{r}}{r} = -e^2 n_s \frac{2\pi}{q} \Big|_{q=0}. \quad (\text{B3})$$

Equation (B2) can also be used to evaluate the contribution to  $E_0$  of the last two terms in Eq. (12)

$$\lim_{r \rightarrow 0} \left[ \sqrt{n_s} \Phi(\pi n_s r^2) - \frac{1}{r} \right] = -2\sqrt{n_s}. \quad (\text{B4})$$

Using (B4) and the identity  $\mathbf{G} = 2\pi n_s (\hat{z} \times \mathbf{R})$ , where  $\hat{z}$  is a unit vector normal to the layers,  $E_0$  reduces finally to Eq. (14), which is equal to Eq. (2.15) of Ref. 19.  $E_0/2$  gives the static energy per electron of a SLWC of density  $n_s$ .

The divergent term in  $E_I$  is

$$\begin{aligned} e^2 \sqrt{n_s} \Psi \left( \frac{G^2}{4\pi n_s}, \pi \eta^2 \right) \Big|_{G=0} &= \frac{e^2 \pi n_s}{G} \left\{ \left[ e^{G\eta/\sqrt{n_s}} + e^{-G\eta/\sqrt{n_s}} \right] \right. \\ &\quad \left. - \left[ e^{G\eta/\sqrt{n_s}} \operatorname{erf} \left( \frac{G}{2\sqrt{\pi n_s}} + \sqrt{\pi} \eta \right) + e^{-G\eta/\sqrt{n_s}} \operatorname{erf} \left( \frac{G}{2\sqrt{\pi n_s}} - \sqrt{\pi} \eta \right) \right] \right\} \Big|_{G=0}. \end{aligned} \quad (\text{B5})$$

The second term on the rhs takes the limit

$$-2e^2\pi n_s \left[ \frac{e^{-\pi\eta^2}}{\pi\sqrt{n_s}} + \frac{\eta}{\sqrt{n_s}} \operatorname{erf}(\sqrt{\pi}\eta) \right], \quad (\text{B6})$$

for  $G \rightarrow 0$ . The first term on the rhs of (B5) can be rewritten

$$e^2\pi n_s \left[ \frac{2e^{-G\eta/\sqrt{n_s}}}{G} + \frac{e^{G\eta/\sqrt{n_s}} - e^{-G\eta/\sqrt{n_s}}}{G} \right]_{G=0} = e^2 n_s \frac{2\pi}{G} e^{-G\eta/\sqrt{n_s}} \Big|_{G=0} + 2e^2\pi\sqrt{n_s}\eta. \quad (\text{B7})$$

Again, the divergent term on the rhs is independent of the lattice geometry and can be neglected. In fact, this term is exactly balanced by the interaction energy of an electron with a positive background charge located at the opposite layer

$$E_I^b = -e^2 n_s \int \frac{d\mathbf{r}}{(r^2 + d^2)^{1/2}} = -e^2 n_s \frac{2\pi}{k} e^{-k\eta/\sqrt{n_s}} \Big|_{k=0}, \quad (\text{B8})$$

which balances the divergency. Therefore, we obtain

$$e^2\sqrt{n_s}\Psi\left(\frac{G^2}{4\pi n_s}, \pi\eta^2\right)_{G=0} = 2e^2\sqrt{n_s} \left\{ \pi\eta \operatorname{erfc}(\sqrt{\pi}\eta) - e^{-\pi\eta^2} \right\}, \quad (\text{B9})$$

and, finally, Eq. (15).

The background charge does not need to sit in the same layer of the mobile electrons. This would be, in fact, the situation in the 2D electron gas realized in semiconductor heterostructures, where the positive ions sit far from the inversion layer. In this case the electrostatic energy has an additional contribution  $2\pi e^2 n_s (d' + d'')$ , where  $d'$ ,  $d''$  are the distances between the compensating layers and the electron layers. Since this additional contribution does not depend on the inter-layer distance  $d$  nor on the lattice structure, it can be neglected.

## REFERENCES

- \* Present address: Department of Physics, University of Modena, Via Campi 213/A, 41100 Modena, Italy. E-mail address: goldoni@unimo.it.
- † E-mail address: peeters@uia.ua.ac.be.
- <sup>1</sup> See, for example, A. Isihara, Solid State Phys. **42**, 271 (1989).
- <sup>2</sup> C. C. Grimes and G. Adams, Phys. Rev. Lett. **42**, 795 (1979).
- <sup>3</sup> C. A. Murray and D. M. Winkle, Phys. Rev. Lett. **58**, 1200 (1987); F. M. Peeters and X. Wu, Phys. Rev. B **35**, 3109 (1987).
- <sup>4</sup> For a recent review, see, for example, R. G. Clark, Physica Scripta **T39**, 45 (1991).
- <sup>5</sup> See, for example, K. J. Strandburg, Rev. Mod. Phys. **60**, 161 (1988).
- <sup>6</sup> M. Kosterlitz and D. Thouless, J. Phys. C **6**, 1181 (1973).
- <sup>7</sup> B. I. Halperin and D. R. Nelson, Phys. Rev. Lett. **41**, 121 (1978); *ibid.* E **41**, 519 (1978).
- <sup>8</sup> A. P. Young, Phys. Rev. B **19**, 1855 (1979).
- <sup>9</sup> Y. M. Vil'k and Y. P. Monarkha, Sov. J. Low Temp. Phys. **10**, 465 (1984) [Fiz. Nizk. Temp. **10**, 886 (1984)].
- <sup>10</sup> Y. M. Vil'k and Y. P. Monarkha, Sov. J. Low Temp. Phys. **11**, 535 (1985) [Fiz. Nizk. Temp. **11**, 971 (1985)].
- <sup>11</sup> V. I. Falko, Phys. Rev. B **49**, 7774 (1994).
- <sup>12</sup> K. Esfarjani and Y. Kawazoe, J. Phys.: Condens. Matter **7**, 7217 (1995).
- <sup>13</sup> G. Goldoni, V. A. Schweigert, and F. M. Peeters, to appear in Surf. Sci. (Proceedings of the EP2DS-XI conference, Nottingham, August 1995).
- <sup>14</sup> S. Narasimhan and T.-L. Ho (unpublished).
- <sup>15</sup> A. Chan and A. H. Mac Donald (unpublished).
- <sup>16</sup> Y. W. Suen, L. W. Engel, M. B. Santos, M. Shayegan, and D. C. Tsui, Phys. Rev. Lett. **68**, 1379 (1992).
- <sup>17</sup> X. M. Chen and J. J. Quinn, Phys. Rev. B **47**, 3999 (1993).
- <sup>18</sup> V. M. Bedanov, G. V. Gadiyak, Y. E. Lozovik, Phys. Lett. **109A**, 289 (1985).
- <sup>19</sup> L. Bonsall and A. A. Maradudin, Phys. Rev. B **15**, 1959 (1977).
- <sup>20</sup> D. S. Fisher, Phys. Rev. B **26**, 5009 (1982).
- <sup>21</sup> See, for example, A. A. Maradudin, E. W. Montroll, G. H. Weiss, and I. P. Ipatova, *Theory of lattice dynamics in the harmonic approximation*, in Solid State Physics, Advances in Research and Applications, Supplement 3, Eds. H. Ehrenreich, F. Seitz, and D. Turnbull (Academic Press, New York, 1971).
- <sup>22</sup> See, for example, D. C. Wallace, *Thermodynamics of crystals* (John Wiley & Sons, New York, 1972).
- <sup>23</sup> M. Saitoh, Phys. Rev. B **40**, 810 (1989).
- <sup>24</sup> M. O. Robbins, K. Kremer, and G. S. Grest, J. Chem. Phys. **88**, 3286 (1988).
- <sup>25</sup> R. H. Morf, Phys. Rev. Lett. **43**, 931 (1979).
- <sup>26</sup> J. P. Eisenstein, G. S. Boebinger, L. N. Pfeiffer, K. W. West, and S. He, Phys. Rev. Lett. **68**, 1383 (1992).
- <sup>27</sup> J. M. Ziman, *Principles of the theory of solids* (Cambridge University Press, U.K., 1972).

## FIGURES

FIG. 1. Static energy per particle of phases I, III, and V. In the insets we show the corresponding lattice geometries in which dots and crosses identify the two sub-lattices.  $\mathbf{a}_1$  and  $\mathbf{a}_2$  are given in Table I.

FIG. 2. Detail of Fig. 1 showing the transitions: (a) I $\rightarrow$ II $\rightarrow$ III, and (b) III $\rightarrow$ IV $\rightarrow$ V. Also shown are the lattice geometries in which full dots and crosses identify the two sub-lattices. Empty dots and diamonds which indicate the sub-lattices of phases I (a) and III (b) are also reported for reference. The insets show how: (a) the aspect ratio  $a_2/a_1$ , and (b) the sine of the angle  $\theta$  between  $\mathbf{a}_1$  and  $\mathbf{a}_2$  evolve during the transition.

FIG. 3. Phonon dispersion curves for phase I (top panel), phase III (middle panel), and phase V (bottom panel), and for several values of  $\eta$ , as indicated in the legends. Phonon frequencies are shown along high symmetry directions in the Brillouin zones of the three phases. In each panel, high symmetry points along the abscissa are labeled according to the insets. Frequencies are given in terms of the characteristic frequency  $\omega_1^2 = e^2 n^{3/2}/m_e$ .

FIG. 4. Sound velocity of the TA mode ( $\omega_1^2 = e^2 n^{3/2}/m_e$ ) along the (1,0) (solid lines) and (1,1) (dashed lines) directions for the five phases. The sound velocity of phase V is isotropic and the two curves coincide. Vertical dotted lines indicate the phase boundaries, according to Figs. 1 and 2; the labels on top of the figure indicate which phase is energetically favoured in each region.

FIG. 5. T=0 phase boundaries (solid dots) and range of stability (crosses) of the five phases along the  $\eta$  axis.

FIG. 6. Optical frequencies at the  $\Gamma$  point for the five phases. For each phase,  $\omega_{opt}$  are reported in the whole range in which the phase is stable. Vertical dotted lines indicate the phase boundaries; the labels on top of the figure indicate which phase is energetically favoured in each region.

FIG. 7. Phonon DOS as a function of frequency for different values of  $\eta$ . For each value of  $\eta$ , the DOS corresponding to the energetically favoured lattice is reported. Dashed lines indicate that a “soft” phase (either II or IV) is stable at that value of  $\eta$ .  $\omega_1^2 = e^2 n^{3/2}/m_e$ .

FIG. 8. Melting temperature  $T_M$  for the five phases. For the “soft” phases II and IV (dashed lines) we used the value of the continuously changing parameter, either the aspect ratio  $a_2/a_1$  or the angle between  $\mathbf{a}_1$  and  $\mathbf{a}_2$ , respectively, for which the energy is at its minimum at T=0.

FIG. 9. Same as Fig. 8, but with  $T_M$  plotted in units of  $(k_B d/e^2 \sqrt{\pi})^{-1}$ .

# TABLES

TABLE I. Lattice parameters of the five geometries considered.  $a$  is the NN distance. For each phase, the primitive vectors  $\mathbf{a}_1$  and  $\mathbf{a}_2$ , the inter-lattice displacement  $\mathbf{c}$ , the reciprocal lattice vectors  $\mathbf{b}_1$  and  $\mathbf{b}_2$ , and the charge density  $n_s$  are indicated. For phase II,  $a_2/a_1$  is the aspect ratio. For phase IV,  $\theta$  is the angle between  $\mathbf{a}_1$  and  $\mathbf{a}_2$ .

Phase	$\mathbf{a}_1/a$	$\mathbf{a}_2/a$	$\mathbf{c}$	$\mathbf{b}_1/(2\pi/a)$	$\mathbf{b}_2/(2\pi/a)$	$n_s a^2$
I–One-component hexagonal	(1, 0)	(0, $\sqrt{3}$ )	$(\mathbf{a}_1 + \mathbf{a}_2)/2$	(1, 0)	(0, $1/\sqrt{3}$ )	$1/\sqrt{3}$
II–Staggered rectangular	(1, 0)	(0, $a_2/a_1$ )	$(\mathbf{a}_1 + \mathbf{a}_2)/2$	(1, 0)	(0, $a_1/a_2$ )	$a_1/a_2$
III–Staggered square	(1, 0)	(0, 1)	$(\mathbf{a}_1 + \mathbf{a}_2)/2$	(1, 0)	(0, 1)	1
IV–Staggered rhombic	(1, 0)	$(\cos \theta, \sin \theta)$	$(\mathbf{a}_1 + \mathbf{a}_2)/2$	$(1, -\cos \theta / \sin \theta)$	$(0, 1 / \sin \theta)$	$1 / \sin \theta$
V–Staggered hexagonal	(1, 0)	$(1/2, \sqrt{3}/2)$	$(\mathbf{a}_1 + \mathbf{a}_2)/3$	$(1, -1/\sqrt{3})$	$(0, 2/\sqrt{3})$	$2/\sqrt{3}$

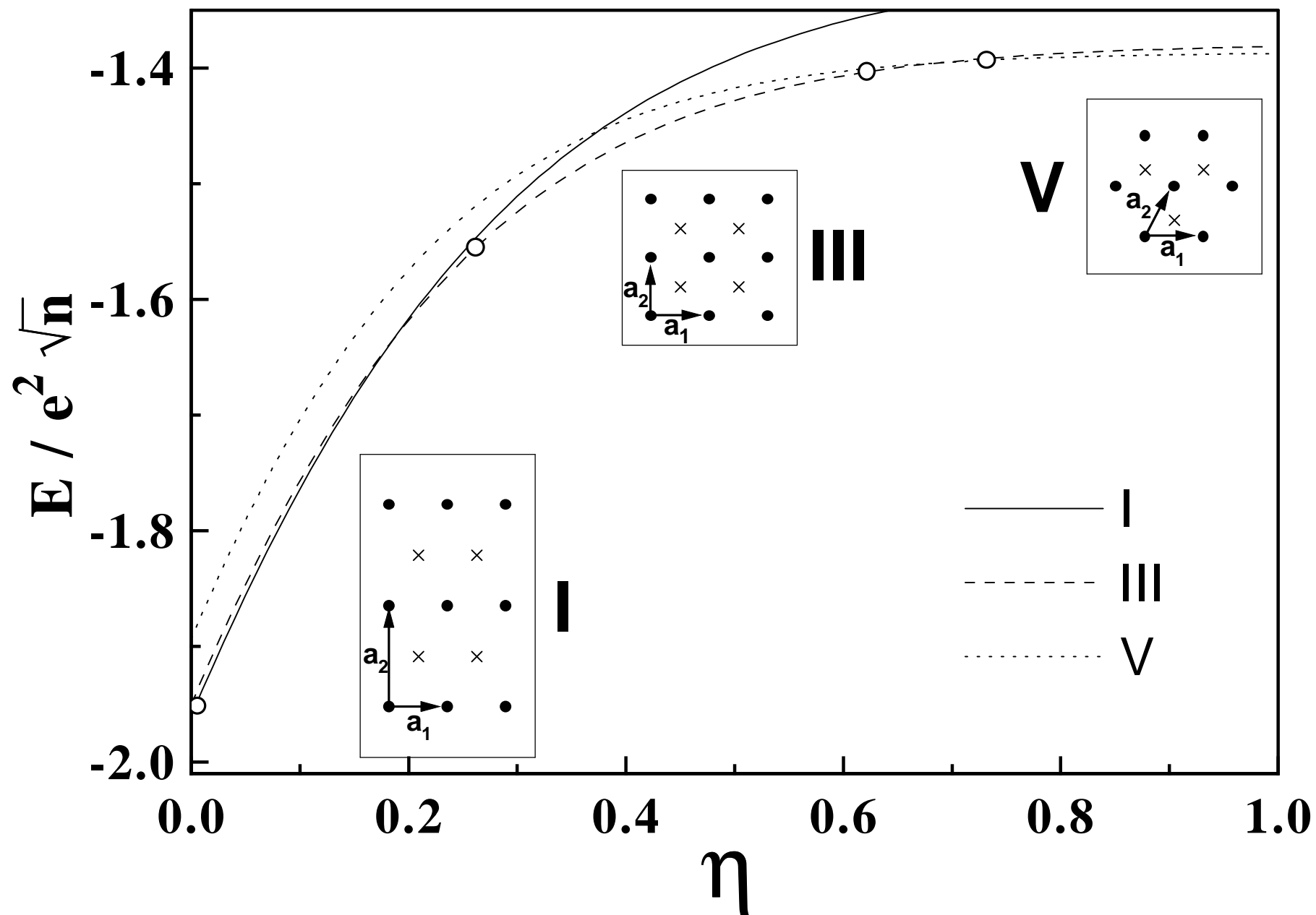
TABLE II. Fitting parameters for the sound velocity  $v_{TA}$  in Eqs.(39) and (40).

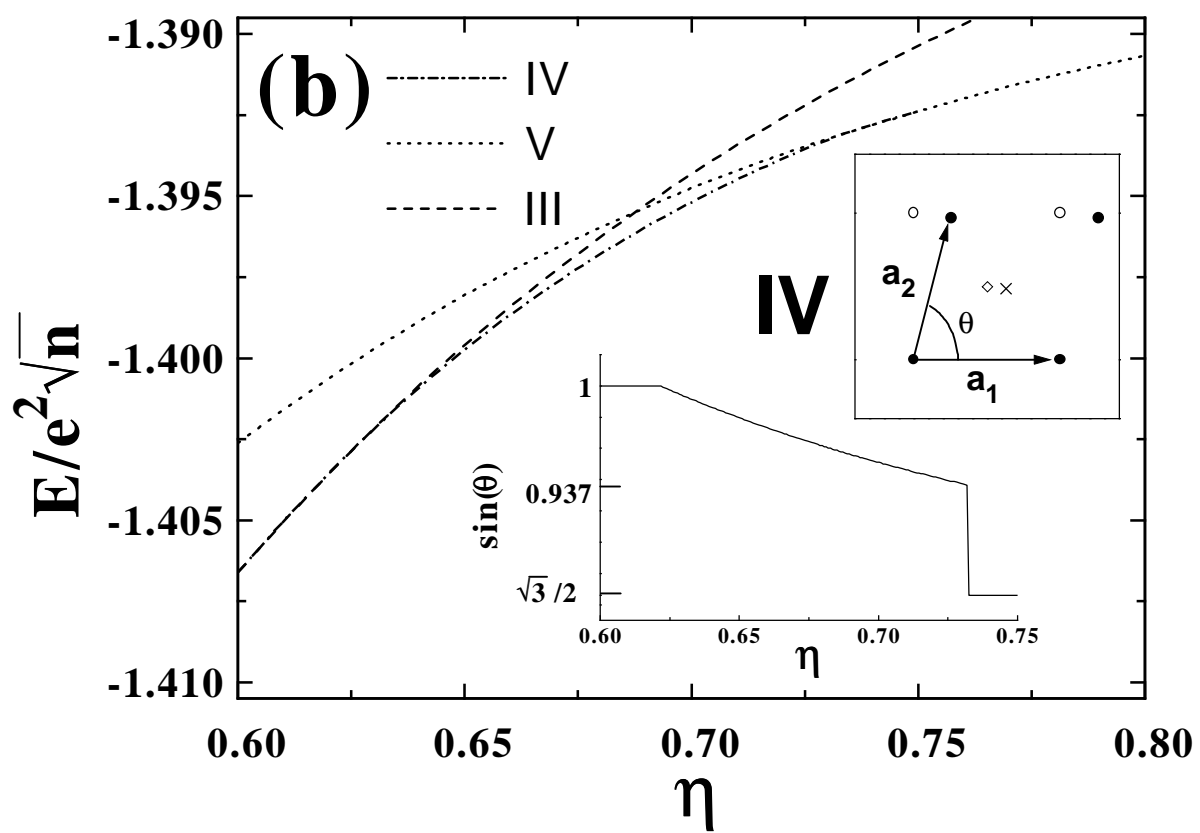
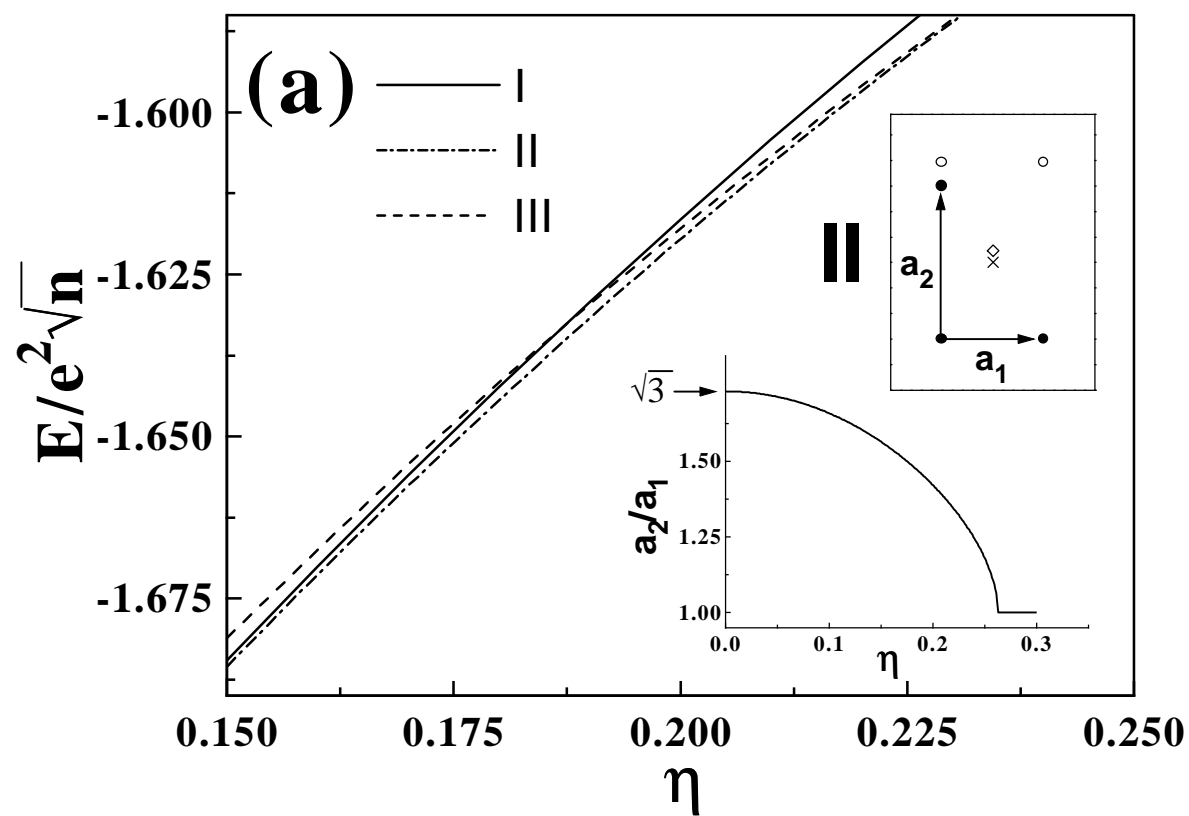
	Small $\eta$ [Eq. (39)]				Large $\eta$ [Eq. (40)]
	Phase I		Phase II		Phase V
	(1,0)	(1,1)	(1,0)	(1,1)	
$p_0$	0.49504		0.49504		0.41628
$p_2$	-3.6871	0.748	1.6608	-3.5072	0.01832
$p_4$	-6.1097	-1.0444	1.5212	-21.192	-0.05925

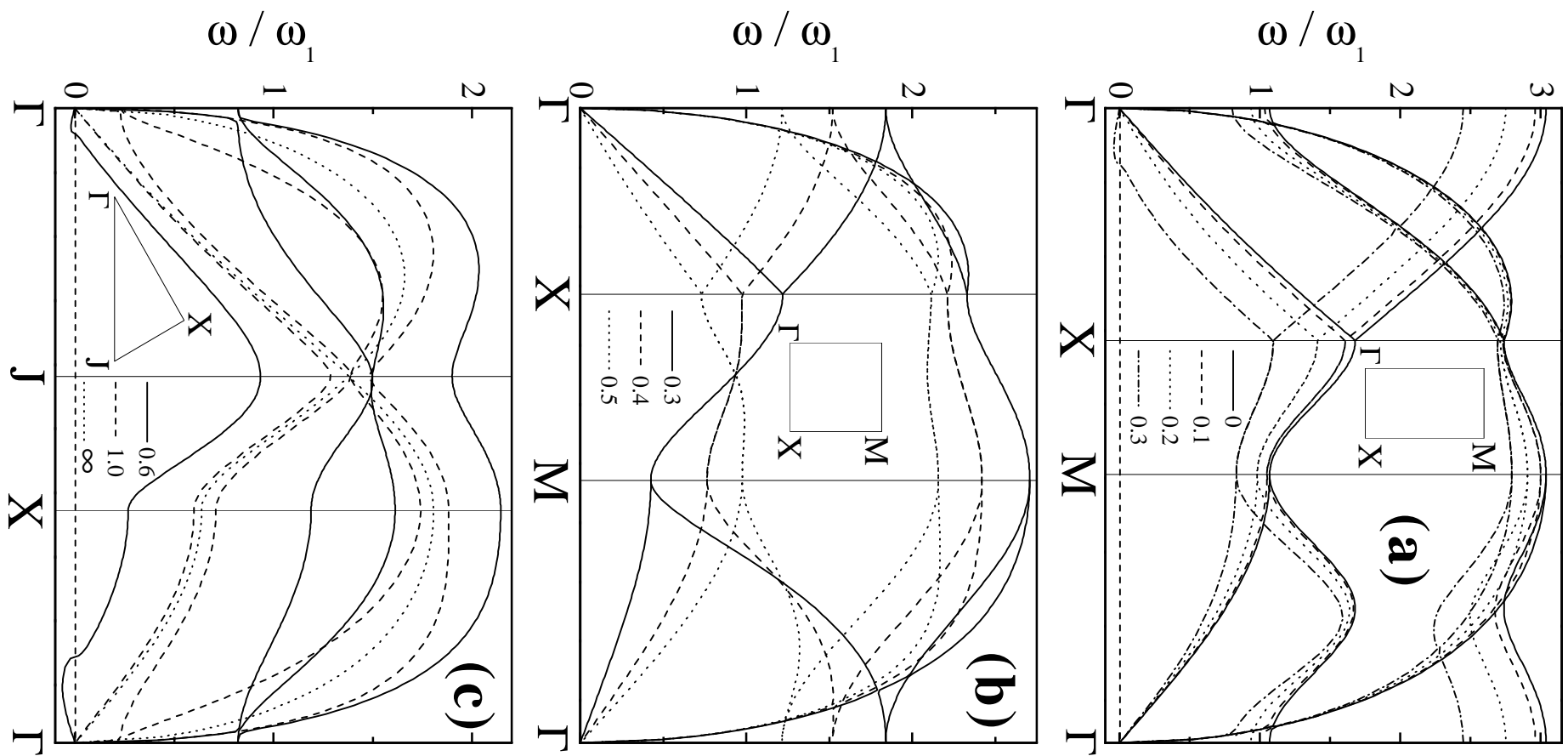
TABLE III. Fitting parameters for the optical frequencies  $\omega_{opt}$  in Eqs.(41), (42), and (43).

Small $\eta$ [Eq. (41)]						Phase boundary [Eq. (43)]		Large $\eta$ [Eq. (42)]
Phase I			Phase II			Phase II		Phase V
Low branch		High branch	Low branch		High branch	Low branch		High branch
$q_0$	1.0706	3.0379	1.0706	3.0379	$q_0$	1.9549		
$q_2$	-3.5818	-7.6876	5.8313	-8.2276	$q_1$	-2.0696	2.6527	5.7169
$q_4$	6.6545	12.742	38.141	-44.859	$q_2$	0.26252	0.26252	3.2168
					$q_3$	0.45103	0.48989	

Goldoni et al. "Stability, dynamical properties, ..." - Fig. 1



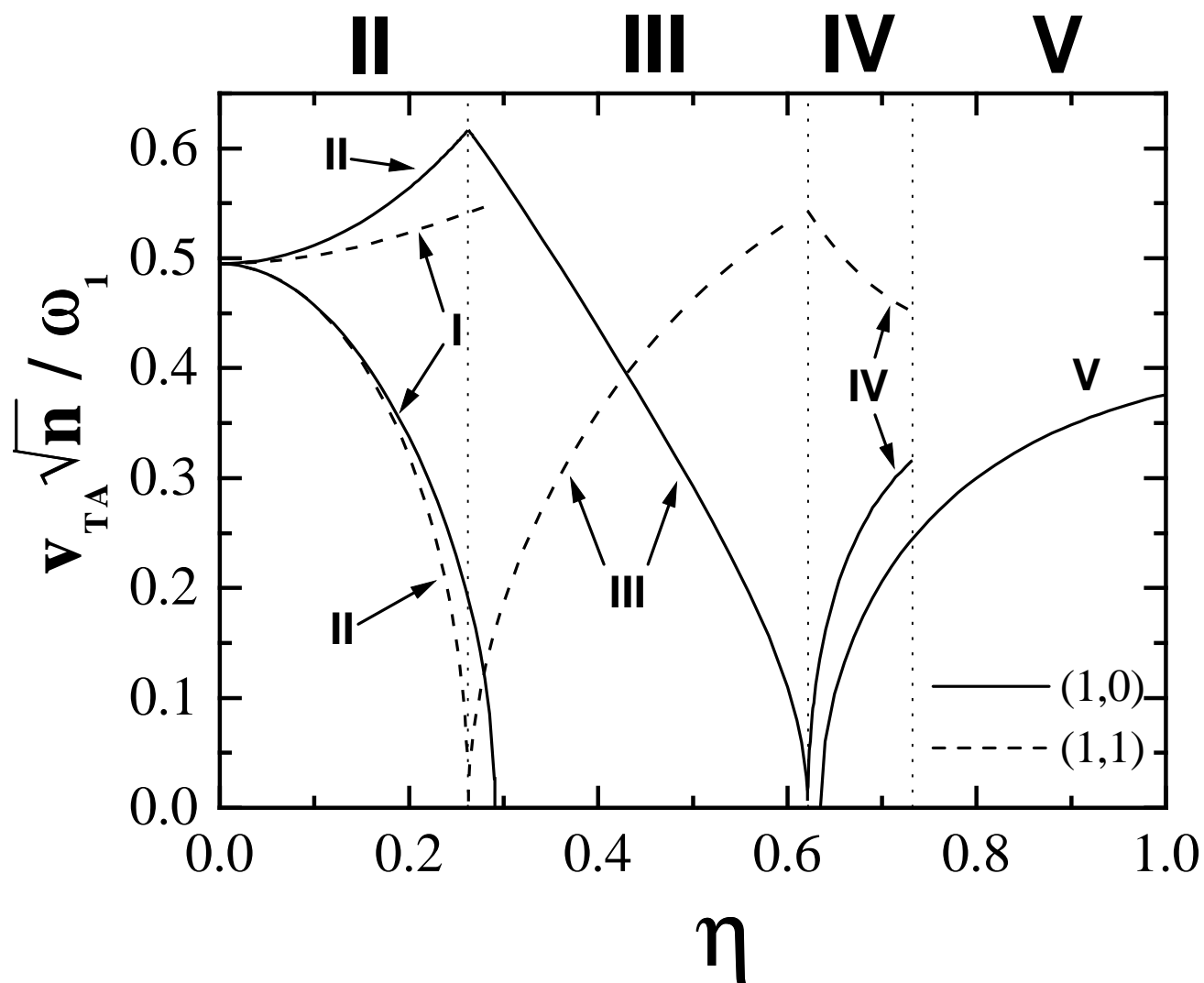




Goldoni et al.

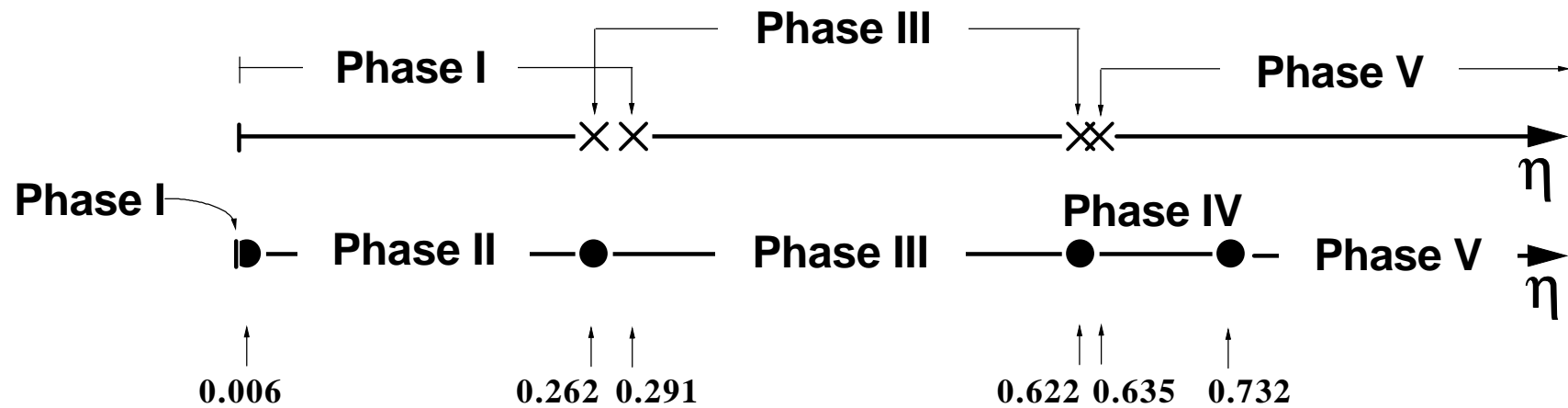
"Stability, dynamical properties, ..." - Fig. 3





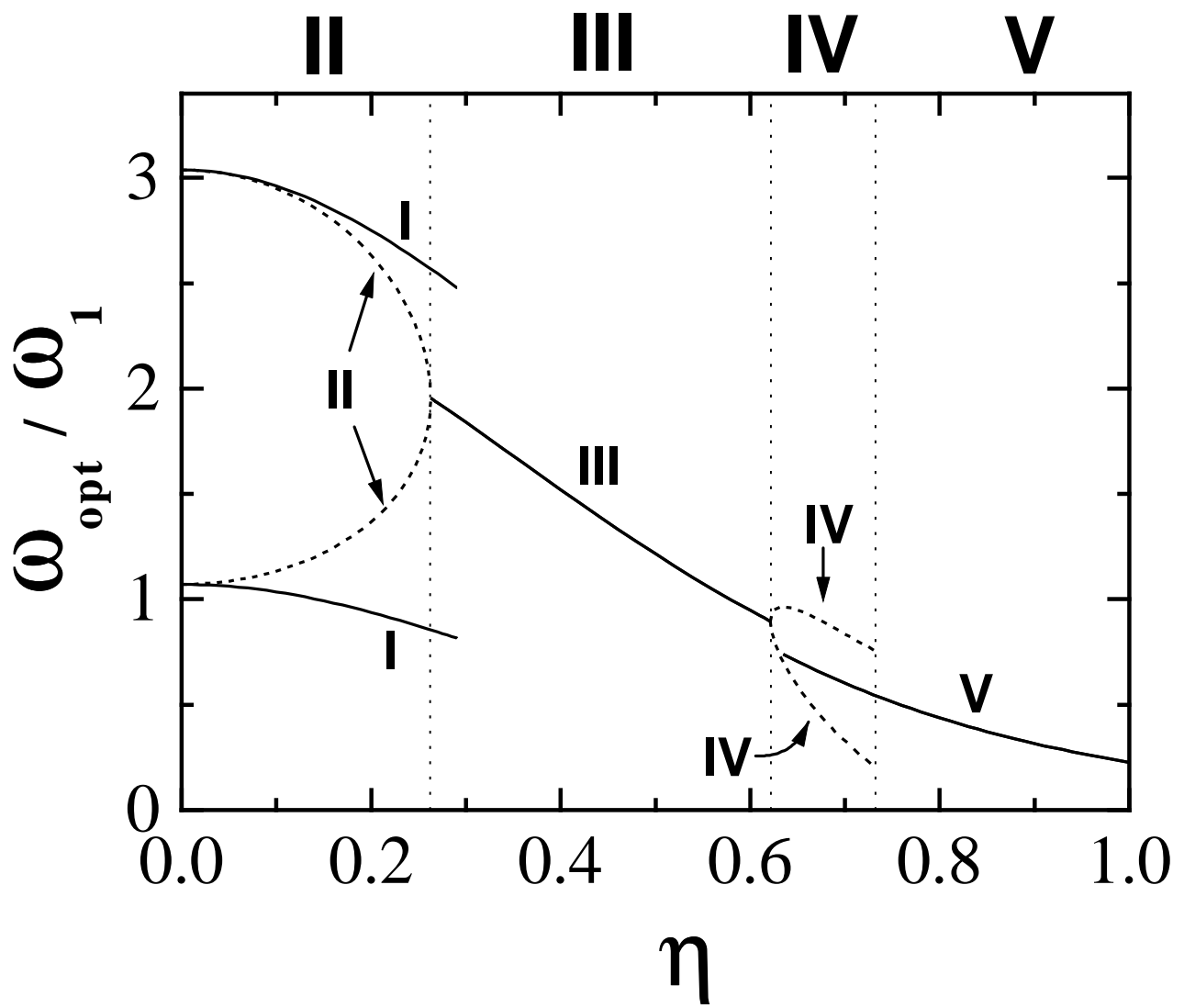
Goldoni et al.

"Stability, dynamical properties, ..." - Fig. 4



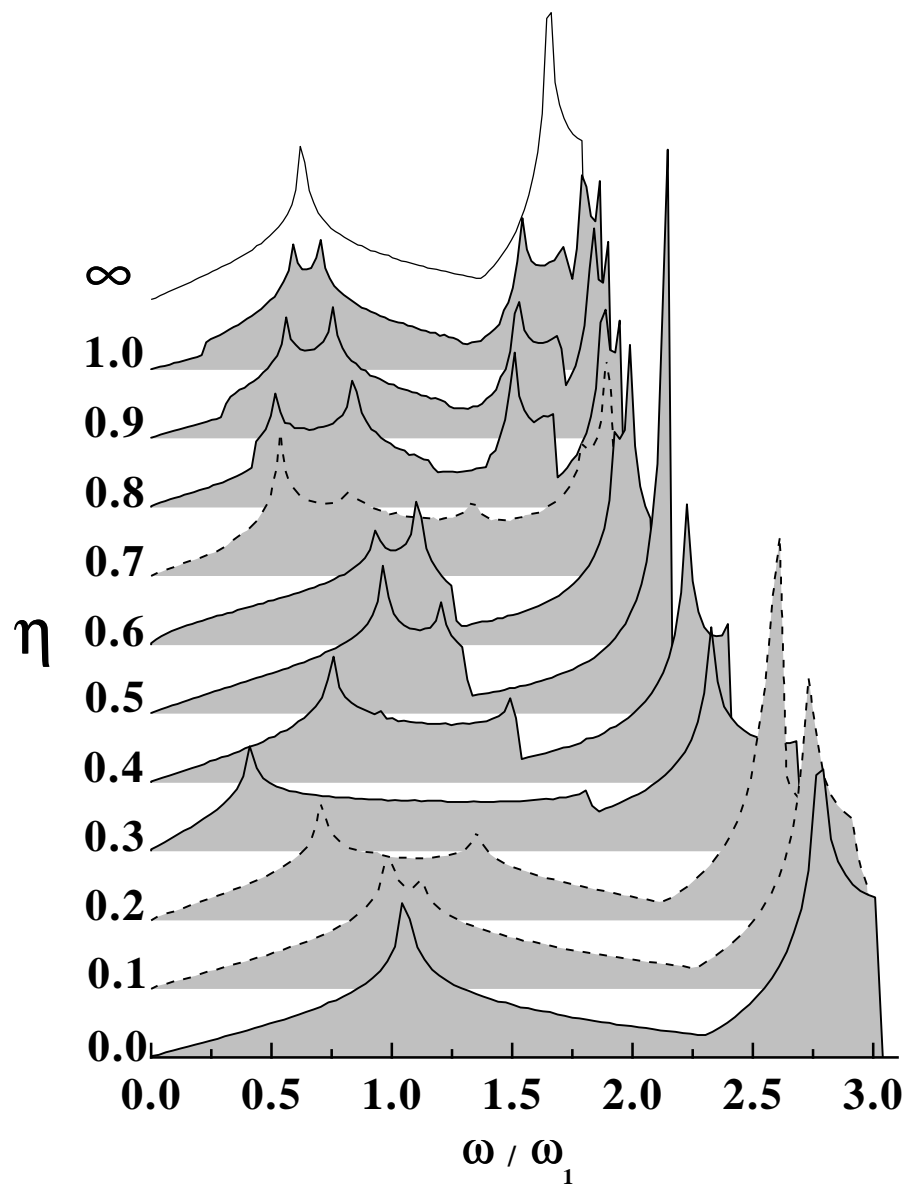
Goldoni et al.

"Stability, dynamical properties, ..." - Fig. 5



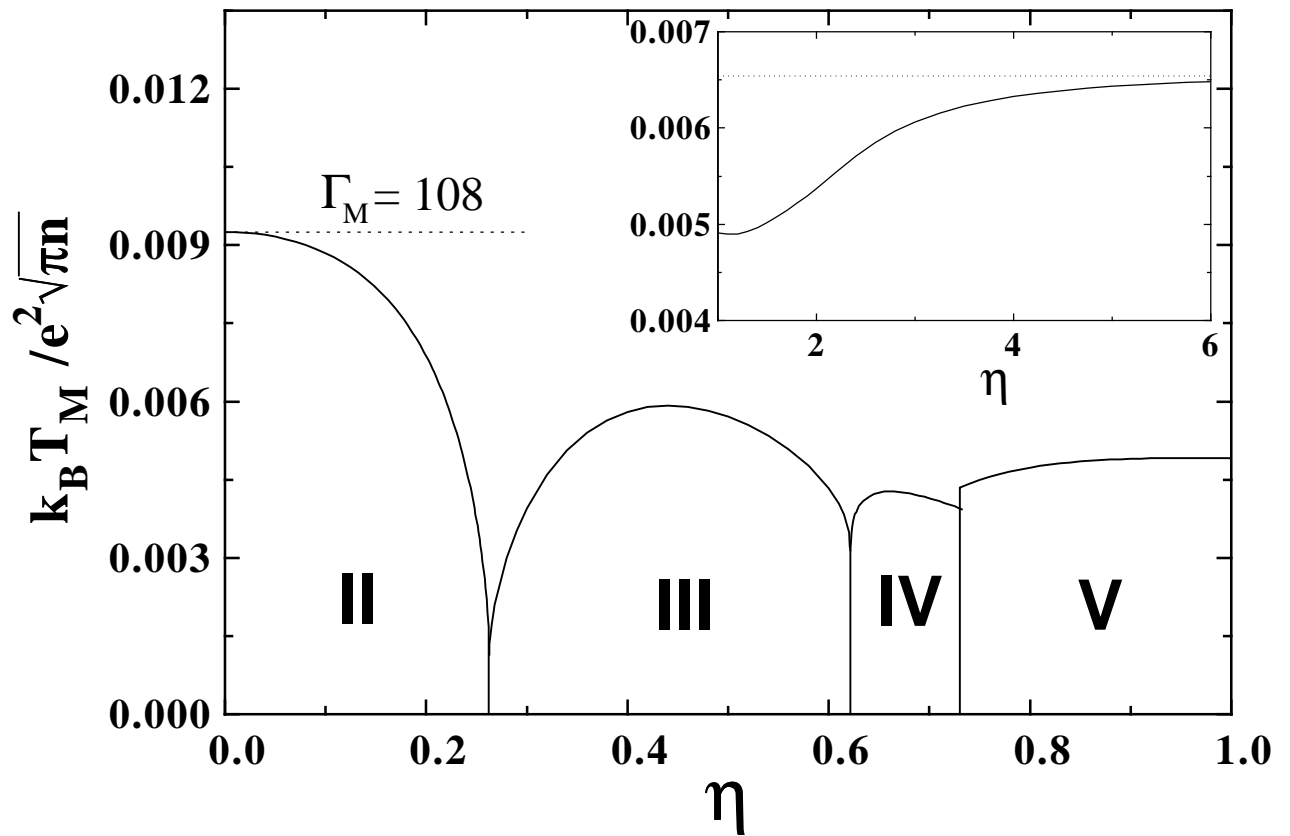
Goldoni et al.

"Stability, dynamical properties, ..." - Fig. 6



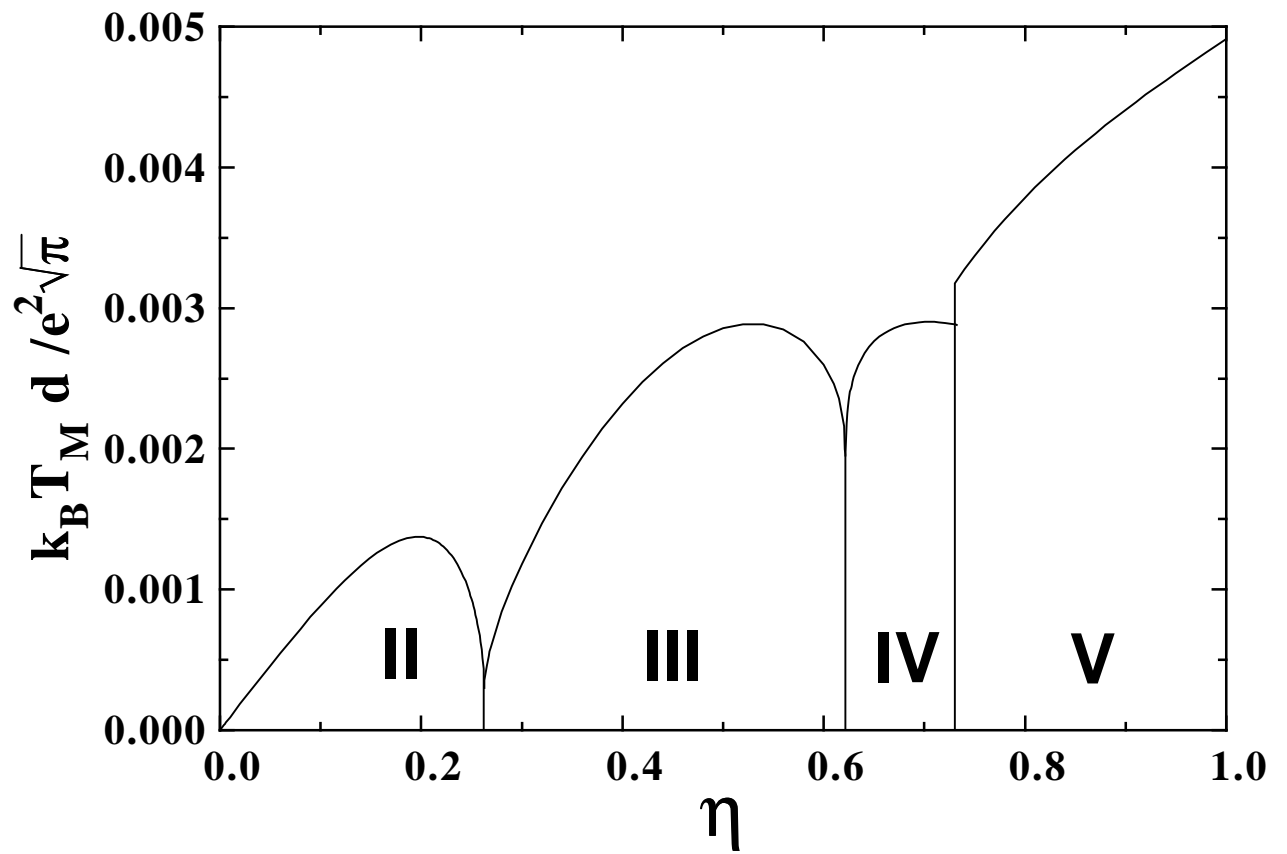
Goldoni et al.

"Stability, dynamical properties, ..." - Fig. 7



Goldoni et al.

"Stability, dynamical properties, ..." - Fig. 8



Goldoni et al.

"Stability, dynamical properties, ..." - Fig. 9